ARTICLES
https://doi.org/10.1038/s41551-020-0547-4

nature biomedical engineering

Ultrabright fluorescent nanoscale labels for the femtomolar detection of analytes with standard bioassays

Jingyi Luan[1], Anushree Seth[1], Rohit Gupta[1], Zheyu Wang[1], Priya Rathi[1], Sisi Cao[1], Hamed Gholami Derami[1], Rui Tang[2], Baogang Xu[2], Samuel Achilefu[2], Jeremiah J. Morrissey[3,4] and Srikanth Singamaneni[1,4] ✉

The detection and quantification of low-abundance molecular biomarkers in biological samples is challenging. Here, we show that a plasmonic nanoscale construct serving as an 'add-on' label for a broad range of bioassays improves their signal-to-noise ratio and dynamic range without altering their workflow and readout devices. The plasmonic construct consists of a bovine serum albumin scaffold with approximately 210 IRDye 800CW fluorophores (with a fluorescence intensity approximately 6,700-fold that of a single 800CW fluorophore), a polymer-coated gold nanorod acting as a plasmonic antenna and biotin as a high-affinity biorecognition element. Its emission wavelength can be tuned over the visible and near-infrared spectral regions by modifying its size, shape and composition. It improves the limit of detection in fluorescence-linked immunosorbent assays by up to 4,750-fold and is compatible with multiplexed bead-based immunoassays, immunomicroarrays, flow cytometry and immunocytochemistry methods, and it shortens overall assay times (to 20 min) and lowers sample volumes, as shown for the detection of a pro-inflammatory cytokine in mouse interstitial fluid and of urinary biomarkers in patient samples.

Relevant concentrations of biomolecules or biomarkers related to diseases such as cancer, heart disease, inflammation and neurological disorders can range in many orders of magnitude from $\mu g\,ml^{-1}$ levels to sub-$fg\,ml^{-1}$, some of which possibly still remain unidentified due to the lack of sensitive bioanalytical tools[1–7]. It is also highly desirable to utilize small sample volume for multiplexed detection within precious biofluids such as breath condensates, ocular fluids, cerebrospinal fluid, or serum from neonates or small animal models, which necessitates sample dilutions, further lowering the concentration. As the cornerstone of biomedical science and clinical research, fluorescence-based bioanalytical methods are widely employed in the detection, quantification and imaging of a broad range of bioanalytes[8–11]. Several methods, such as enhancing antibody affinity[12], reducing the background fluorescence[13], promoting mass transfer[14] and increasing the substrate surface area[8,14], have been explored to improve the sensitivity of fluoroimmunoassays. However, the weak fluorescence signal and the associated poor signal-to-noise ratio of the fluorescence label remains a persistent challenge, limiting the ultimate sensitivity of current fluorescence-based assays[10,15–17].

Extensive efforts have been dedicated to creating a bright fluorescence signal that involves the conversion of a single molecular event into thousands (or more) of fluorophores in a localized 'enzyme free' manner[18–24]. Achieving ultrabright nanostructures by simply packing a large number of fluorophores into a nanoscale volume is extremely challenging due to the aggregation-induced self-quenching of fluorophores at high local concentration, limiting the fluorophore loading and consequently their brightness[21,25]. One solution to prevent the formation of non-emissive H-aggregates is to engineer the interfluorophore distance and orientation, for example, by modifying the fluorophore with bulky side groups[26,27] or using charged dyes with hydrophobic counterions[18]. However, the loading is still limited to tens or hundreds of fluorophores per nanoparticle in these cases. Fluorescent nanoparticles based on Förster resonance energy transfer represents an attractive method that can harvest incident light and transfer it to adjacent energy acceptors. However, limited by the Förster radius (typically much shorter than the radius of nanostructure, which hinders the efficient energy transfer from a whole nanoparticle to the energy acceptor) and self-quenching of donors at high local concentration, efficient Förster resonance energy transfer system (1,000-fold brighter than a single fluorophore) was not demonstrated until recently[23,28]. Again, this method is only applicable to charged fluorophores and broad application of these nanostructures in fluorescence-based bioanalytical and bioimaging techniques has not been demonstrated[23].

Here we introduce a stable and bright fluorescent nanoconstruct, termed 'plasmonic-fluor', which exhibits up to 6,700 (±900)-fold (±s.d., this applies to all ±values) brighter signal compared with the corresponding single near-infrared (NIR) fluorophore (800CW, LI-COR), outperforming existing nanoengineered fluorescent structures[18–24]. This nanoconstruct integrates plasmon-enhanced fluorescence, a biolinker element and a bovine serum albumin (BSA) surface-blocking strategy, enabling it to serve as a specific and cross-assay label in various fluorescence-based bioanalytical and imaging methodologies to enhance their signal-to-noise ratios. Harnessing the nanoconstruct (that is, plasmonic-fluor), we show that plasmon-enhanced fluorescence improves the sensitivity of a variety of bioanalytical applications, such as fluorescence-linked

[1]Department of Mechanical Engineering and Materials Science, Institute of Materials Science and Engineering, Washington University in St. Louis, St Louis, MO, USA. [2]Department of Radiology, Washington University School of Medicine, St. Louis, MO, USA. [3]Department of Anesthesiology, Division of Clinical and Translational Research, Washington University in St. Louis, St. Louis, MO, USA. [4]Siteman Cancer Center, Washington University in St. Louis, St. Louis, MO, USA. ✉e-mail: singamaneni@wustl.edu

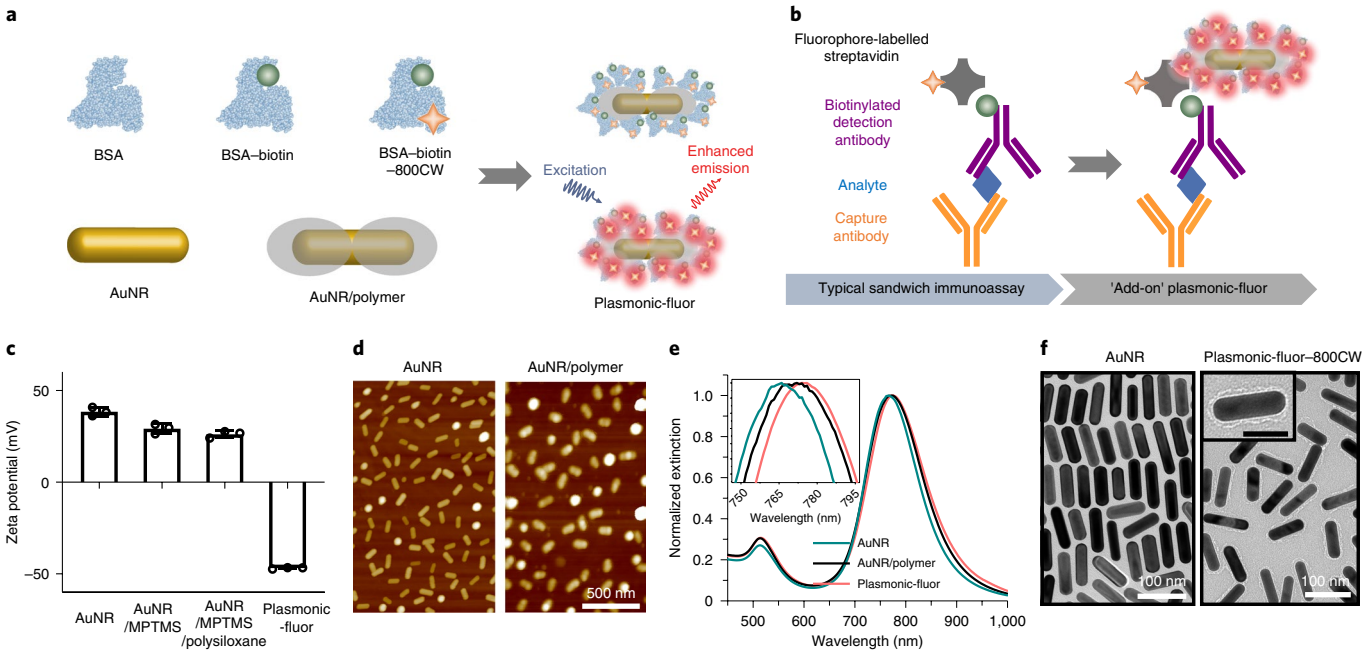

Fig. 1 | Plasmonic-fluor synthesis and material characterization. a, Schematic illustration showing the structure of plasmonic-fluor, which consists of a plasmonically active core (for example, an AuNR), a polymer shell as spacer layer, light emitters and a universal biorecognition element (biotin). BSA is employed as a key design element to assemble all components into the functional nanoconstruct and to resist non-specific binding. **b**, Working principle of plasmonic-fluor as an 'add-on' biolabel to enhance the fluorescence intensity and consequent signal-to-noise ratio of fluorescence-based assays, without changing the existing assay workflow. **c**, Zeta potential of AuNR, AuNR/MPTMS, AuNR/MPTMS/polysiloxane (AuNR/polymer) and the plasmonic-fluor–800CW (AuNR/polymer/BSA–biotin–800CW). Error bars, s.d. ($n=3$ repeated tests). **d**, AFM images showing the AuNR before and after coating with polymer. **e**, Visible–NIR extinction spectra of AuNR, AuNR/polymer and plasmonic-fluor, showing a progressive redshift in the LSPR wavelength after each step. **f**, TEM images of bare AuNR and plasmonic-fluor–800CW.

immunosorbent assays (FLISA), multiplexed bead-based fluoroimmunoassays, high-throughput protein arrays, immunocytochemistry/immunofluorescence (ICC/IF) and flow cytometry.

Plasmonic-fluor synthesis and characterization

Plasmonic-fluor is composed of a plasmonic nanostructure (as a fluorescence enhancer), a light emitter (for example, molecular fluorophores), spacer layer and a universal biological recognition element (for example, biotin) (Fig. 1a). To assemble all of these functional components, we have employed BSA as a scaffold. As a key design element, BSA also serves as (1) a stabilizing agent, preventing the aggregation of the nanoconstructs, and (2) a blocking agent, minimizing non-specific binding of the plasmonic-fluor to arbitrary surfaces and biomolecules, which is extremely important to achieve high signal-to-background ratios. BSA is covalently conjugated with fluorophores and biotin and subsequently coated around the plasmonic nanostructures to realize plasmonic-fluors. The synthesized plasmonic-fluor exhibited strong and specific affinity to streptavidin (a tetrameric biotin-binding protein), owing to the high affinity (dissociation constant (K_d)$\approx 10^{-14}$ mol l^{-1}) of the biotin–streptavidin complex[29]. Streptavidin conjugated with fluorophore is widely used in fluorescence-based bioanalytical techniques as a universal signal reporter. We hypothesized that following the binding of streptavidin, plasmonic-fluor can be introduced as an 'add-on' step to enhance the fluorescence signal without entailing any change in the existing bioassay protocols (Fig. 1b).

Gold nanorods (AuNRs) are employed as representative plasmonic nanoantennae owing to the facile tunability of their longitudinal localized surface plasmon resonance (LSPR) wavelength with aspect ratio and large electromagnetic field enhancement at their ends (Supplementary Fig. 1)[30–32]. AuNRs (length 83.0 ± 8.0 nm; diameter 24.3 ± 1.8 nm) were modified with (3-mercaptopropyl) trimethoxysilane (MPTMS), which served as an interfacial layer for the copolymerization of two organosilane monomers, namely (3-aminopropyl)trimethoxysilane (APTMS) and trimethoxypropylsilane (TMPS) (Supplementary Fig. 2). In aqueous media, APTMS and TMPS undergo rapid hydrolysis and subsequent condensation around the MPTMS-modified AuNRs, yielding an amorphous copolymer network (Supplementary Fig. 2). The siloxane copolymer serves as a spacer layer between the metal surface and the fluorophore to prevent fluorescence quenching (Fig. 1d). This sol–gel approach enables facile control over the thickness of the spacer layer down to 1 nm, as evidenced by atomic force microscopy (AFM) (Supplementary Fig. 3). Modification of AuNRs with MPTMS and subsequent polymerization of APTMS/TMPS reduced the zeta potential of cetyl trimethylammonium bromide (CTAB)-capped AuNRs from +38.4 ± 2.3 mV to +29 ± 2.6 mV and +25.8 ± 1.9 mV, respectively, due to the partial replacement of the positively charged capping agent (CTAB) with the less-charged siloxane copolymer (Fig. 1c).

NIR fluorophore 800CW (LI-COR) and biotin were conjugated to BSA through carbodiimide coupling chemistry to realize conjugates with a protein:biotin:fluorophore ratio of 1:8.7:1.2 (Supplementary Figs. 4 and 5). Subsequently, the BSA–biotin–800CW conjugates are adsorbed on polysiloxane-coated AuNRs through electrostatic, hydrophobic and hydrogen-bonding interactions between BSA and the functional groups (–NH_{3+}, –CH_3, –OH) of the polysiloxane layer to realize plasmonic-fluor–800CW. As-formed plasmonic-fluor–800CW exhibited a negative charge (zeta potential −46.9 ± 0.5 mV at pH 10) due to abundant carboxylic acid groups in BSA with an isoelectric point of 4.7 (Fig. 1c)[33]. The LSPR wavelength of the AuNRs exhibited a progressive redshift of 2.6 nm and 2.7 nm with the formation of the polymer spacer layer and BSA–biotin–800CW adsorption, respectively (Fig. 1e). Transmission electron microscopy

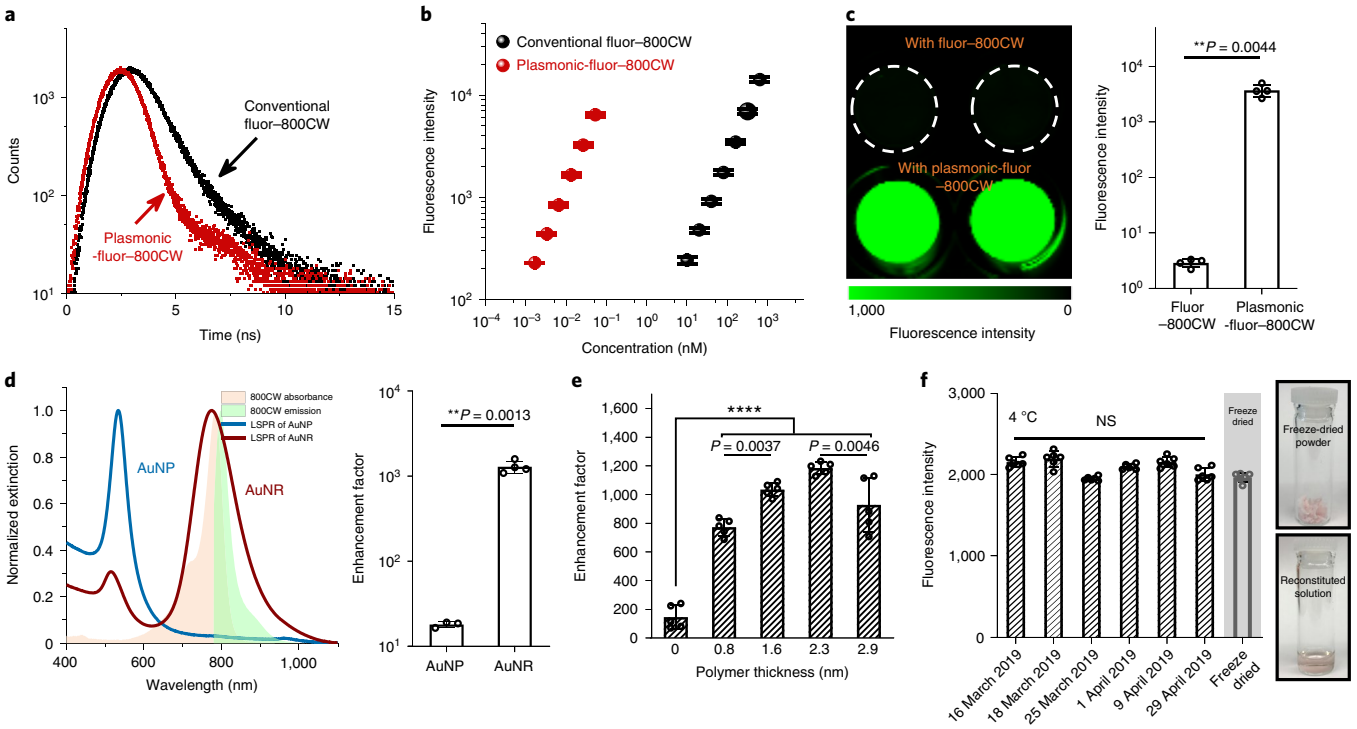

Fig. 2 | Plasmon-enhanced fluorescence and colloidal stability of plasmonic-fluors. a, Excited state lifetime measurements of conventional fluor–800CW and plasmonic-fluor–800CW showing a decrease in the lifetime of 800CW after adsorption on AuNRs. **b**, Fluorescence intensity of conventional fluor–800CW and plasmonic-fluor–800CW at their different molar concentrations. The difference in the slopes of the two curves indicates that a single plasmonic-fluor–800CW is as bright as 6,700 (±900) fluorophores. Error bars, s.d. ($n = 3$ repeated tests). **c**, Fluorescence intensity of 800CW–streptavidin followed by the specific binding of plasmonic-fluor–800CW through biotin–streptavidin interaction, showing an average of 1,200 (±40)-fold increase in fluorescence intensity. Error bars, s.d. ($n = 4$ independent tests). Data statistically significant P value = 0.0044, ** $P < 0.01$ by two-tailed unpaired t-test with Welch's correction. **d**, Left: LSPR wavelength of AuNPs and AuNRs with a similar surface area. The plot also shows the absorption and emission spectra of 800CW. Right: fluorescence enhancement factor upon binding of 'off-resonant' AuNP–plasmonic-fluor–800CW and 'on-resonant' AuNR–plasmonic-fluor–800CW to 800CW–streptavidin. Error bars, s.d. (AuNP group: $n = 3$ independent tests. AuNR group: $n = 4$ independent tests.). Data statistically significant P value = 0.0013, ** $P < 0.01$ by two-tailed unpaired t-test with Welch's correction. **e**, Fluorescence enhancement factor obtained using plasmonic-fluor–800CW with different polymer spacer thickness. Error bars, s.d. ($n = 5$ independent tests). **** $P < 0.0001$ by one-way ANOVA with Tukey's post test. **f**, Left: plot showing the stability of plasmonic-fluor suspension stored at 4 °C and reconstituted from lyophilized powder. Error bars, s.d. ($n = 6$ repeated tests). NS, not significant. P value > 0.9999 by one-way ANOVA with Tukey's post test. Right: photographs depicting the lyophilized powder of plasmonic-fluor before and after reconstitution.

(TEM) images further confirmed the presence of a thin organic layer (polymer and BSA conjugate) around the AuNR with an overall thickness of ~6.3 ± 1.4 nm (Fig. 1f).

Following the structural characterization of plasmonic-fluor–800CW, we set out to determine the brightness of the fluorescent nanoconstruct. The excited state fluorescence lifetimes of free 800CW (conjugated to BSA) and plasmonic-fluor–800CW were measured to be 0.74 ± 0.01 ns and 0.179 ± 0.001 ns, respectively, amounting to a sevenfold increase in the quantum yield (from ~11% (800CW) to ~79% (plasmonic-fluor–800CW), see Supplementary Information for calculation; Fig. 2a and Supplementary Figs. 6 and 7)[34]. To further understand the brightness of plasmonic-fluor–800CW, we estimated the number of fluorophores conjugated to a single AuNR. Plasmonic-fluor–800CW at a concentration of 76.2 pM (extinction of ~0.63) is composed of ~16 nM 800CW (see Supplementary Information for detailed calculation). Therefore, we can estimate that approximately 210 fluorophores are conjugated to a single AuNR. Notably, fluorescence intensity from 76.2 pM plasmonic-fluor–800CW (containing 16 nM 800CW) was found to be equivalent to the fluorescence intensity from 544 nM 800CW (measured based on Fig. 2b). Therefore, it can be concluded that each 800CW is enhanced by nearly 30-fold due to the presence of plasmonic nanoantenna. The slope of fluorescence intensity versus molar concentration of plasmonic-fluor–800CW is 6,700 (±900)-fold steeper than that of the conventional fluorophore (800CW) (Fig. 2b and Supplementary Fig. 8), suggesting that each plasmonic-fluor exhibits 6,700 (±900)-fold higher brightness than the corresponding fluorophore[19,35]. The observed intense emission can be attributed to the enhanced electromagnetic field (local excitation field) at the surface of the plasmonic nanostructures (Supplementary Fig. 1) and decrease in the fluorescence lifetime due to the coupling between excited fluorophores and surface plasmons of the nanostructures[8,10,36–43].

We tested the feasibility of using plasmonic-fluor–800CW as ultrabright fluorescent reporters by binding them to a substrate coated with streptavidin–800CW (see Methods for detailed procedure; Supplementary Fig. 9). Binding of plasmonic-fluor–800CW resulted in an average of 1,200 (±40)-fold increase in the ensemble fluorescence intensity compared with streptavidin–800CW (LI-COR) (Fig. 2c). The signal enhancement was achieved by using a relatively low concentration of the plasmonic-fluors (76 pM). To further validate the plasmonic enhancement of fluorescence, we employed an 'off-resonant' gold nanoparticle (AuNP) with a similar surface area to the 'on-resonant' AuNR (AuNP, 7,850 nm^2; AuNR, 8,064 nm^2) (Supplementary Fig. 10). The AuNPs exhibited an LSPR wavelength around 530 nm, which was 'off-resonant' with respect

to the excitation laser (785 nm) and 800CW emission (800 nm) (Fig. 2d). It is known that a large overlap between LSPR band of the plasmonic nanostructures and the excitation and emission bands of the fluorophores is critical for maximizing the fluorescence enhancement[44]. Not surprisingly, AuNP–plasmonic-fluor–800CW resulted in only 18-fold enhancement in the fluorescence intensity, which is about 70-fold lower than that obtained with AuNR–plasmonic-fluor–800CW, confirming the plasmonically enhanced fluorescence (Fig. 2d).

Our group and others have shown that an optimal distance between the metal surface and fluorophore is critical to maximize fluorescence enhancement by balancing the two opposing factors, namely, enhanced electromagnetic field and non-radiative energy transfer[45–51]. Fluorescence enhancement of plasmonic-fluor–800CW with different thicknesses of the dielectric spacer (MPTMS, APTMS and TMPS) was investigated by binding them to a substrate coated with streptavidin–800CW. The ensemble fluorescence enhancement factor (defined as the ratio of fluorescence intensities obtained after and before the addition of plasmonic-fluors on a surface coated with fluorophore-conjugated streptavidin) of the plasmonic-fluors without a polymer spacer layer was found to be ~146 ± 81. Enhancement efficiency progressively increased to ~1,200 (±40)-fold with increasing spacer thickness (Fig. 2e). Notably, the colloidal solution of plasmonic-fluor exhibited a stable fluorescence signal after storage in the dark at 4 °C for one month (Fig. 2f). For further ease of storage, transportation and handling, the plasmonic-fluors can be lyophilized and reconstituted as needed without noticeable degradation in the fluorescence signal (Fig. 2f).

Plasmonic-fluor-enhanced FLISA and multiplexed bead-based assay

Of the numerous applications of plasmonic-fluors, we first set out to demonstrate plasmon-enhanced FLISA (p-FLISA) implemented on a standard microtitre plate. Human interleukin-6 (IL-6), a pro-inflammatory cytokine, was employed as a representative protein biomarker. Conventional FLISA involves a standard sandwich format of capture antibody, analyte (IL-6), biotinylated detection antibody, followed by exposure to streptavidin–fluorophore (800CW in this study) (Fig. 3a). In p-FLISA, plasmonic-fluor–800CW is introduced after the last step as the signal enhancer (Fig. 3a). To determine the improvement in sensitivity and the limit of detection (LOD, defined as mean + 3σ of the blank), serial dilutions of IL-6 of known concentration (6 ng ml^{-1} to 6 fg ml^{-1}, in 1% BSA buffered with phosphate buffered saline (PBS)) were employed as standards. The fluorescence signal obtained after applying the plasmonic-fluor–800CW revealed nearly 1,440-fold enhancement in the ensemble fluorescence intensity compared with the conventional FLISA at the highest analyte concentration tested here (6 ng ml^{-1}) (Fig. 3b,c and Supplementary Figs. 11 and 12). The LOD of conventional FLISA was calculated to be ~95 pg ml^{-1} (Fig. 3d and Supplementary Figs. 11, and 12, polynomial fit). In contrast, the fluorescence signal with p-FLISA could be detected down to 20 fg ml^{-1} (~1 fM) (Fig. 3e and Supplementary Fig. 12, four-parameter logistic fit), which represents a 4,750-fold improvement in the LOD compared with conventional FLISA. Notably, plasmonic-fluor exhibited extremely high specificity (to streptavidin) and low non-specific binding to the interference biomolecules in the bioassays (Supplementary Fig. 14). We attribute this to the 'BSA blocking' strategy of plasmonic-fluor, which is critical in enhancing the signal-to-background ratio. Scanning electron microscopy (SEM) images revealed an increase in the density of plasmonic-fluor–800CW at the bottom of the microtitre wells with increasing IL-6 concentration (Supplementary Fig. 15). An extremely low density of plasmonic-fluors was observed in the blank well, which was incubated with 1% BSA, again indicating the low non-specific binding of the plasmonic-fluors (Supplementary Fig. 15).

The LOD and lower limit of quantification (LLOQ, defined as mean + 10σ of the blank, ~82 fg ml^{-1}) of p-FLISA were found to be 189-fold and 120-fold lower than the 'gold standard' enzyme-linked immunosorbent assay (ELISA), which involves enzymatic amplification of the colorimetric signal (Fig. 3c,f and Supplementary Fig. 12). More importantly, p-FLISA exhibited a dynamic range (ratio between higher and LLOQ) of five orders of magnitude, which is more than two orders of magnitude higher than that of ELISA. As a validation of the assay performance, we have tested healthy human serum samples and IL-6 spiked serum using p-FLISA. Serum samples were diluted by tenfold so that only 10 µl of original sample was required for individual subjects. Concentrations of IL-6 in healthy individuals are normally in the range of 0.2–7.8 pg ml^{-1} (ref. [52]). An increased level of IL-6 in serum can be indicative of systemic inflammatory, metabolic and physiological stimuli[52]. Notably, among ELISA, FLISA and p-FLISA, only the latter technique was able to determine the IL-6 concentration in healthy individuals, which were measured to be 8.1, 1.8 and 2.8 pg ml^{-1} after dilution-fold correction, respectively (Fig. 3g).

Harnessing the high sensitivity and large dynamic range, we demonstrate that p-FLISA can be employed as a biomedical research tool to quantitatively analyse biomarkers in precious biofluids of extremely small volume (as low as 10 nl), such as interstitial fluid (ISF). One of the existing challenges in ISF analysis is the inadequate amount of ISF that can be extracted using the existing techniques, making downstream proteomic and metabolomic analysis challenging[53]. Here we employed p-FLISA to measure the concentrations of IL-6 in dermal ISF obtained from mice that were immune-stimulated with lipopolysaccharide (LPS) and naïve mice (as controls). It is important to note that only a small amount of ISF (less than 10 µl) could be obtained from the entire skin from the back of the mice (~6 cm^2) (Supplementary Fig. 16a). To determine the smallest amount of sample required for p-FLISA and conventional ELISA, mouse ISF was diluted 100-fold, 1,000-fold, 10,000-fold and 100,000-fold (representing 1 µl, 0.1 µl, 0.01 µl and 0.001 µl of ISF for each test zone, respectively) and assayed with both methods. The large dynamic range of p-FLISA enabled the detection and quantification of IL-6 concentrations in ISF samples at all the dilutions from immune-stimulated mice (Supplementary Fig. 16b). Moreover, the high sensitivity of p-FLISA also enabled the detection and quantification of IL-6 concentrations in ISF from naïve mice, which was measured to be three orders of magnitude lower compared with immune-stimulated mice group (Supplementary Fig. 16c). Compared with p-FLISA, conventional ELISA (with ~100-fold inferior LOD of ~11.2 pg ml^{-1}) required a 100-fold larger sample volume. The IL-6 in immune-stimulated mouse ISF of high dilution (>1,000-fold) and in healthy mouse ISF cannot be detected using standard ELISA (Supplementary Fig. 16d).

To further demonstrate the translational potential of plasmonic-fluor in clinical diagnostic settings, we show that p-FLISA can shorten the overall sample-to-answer time, making them attractive for point-of-care applications. In many pathological conditions, such as acute kidney injury, myocardial infarction and sepsis, shortening the time to treatment is critical to improve the clinical outcomes. The large enhancement in the fluorescence intensity and signal-to-noise ratio of p-FLISA allows us to shorten the overall assay time to 20 min. The ultrafast p-FLISA (20 min) exhibited the same sensitivity as the conventional ELISA (280 min) (Supplementary Fig. 17a,b), in measuring the concentrations of urinary neutrophil gelatinase-associated lipocalin (NGAL), which can be elevated above normal level in patients with renal masses and kidney diseases such as acute kidney injury and chronic kidney disease[54,55]. The ultrafast p-FLISA was able to accurately quantify the urinary NGAL concentrations from ten patients with imaged renal masses and ten self-described healthy individuals and the assay revealed NGAL concentrations in patients to be higher

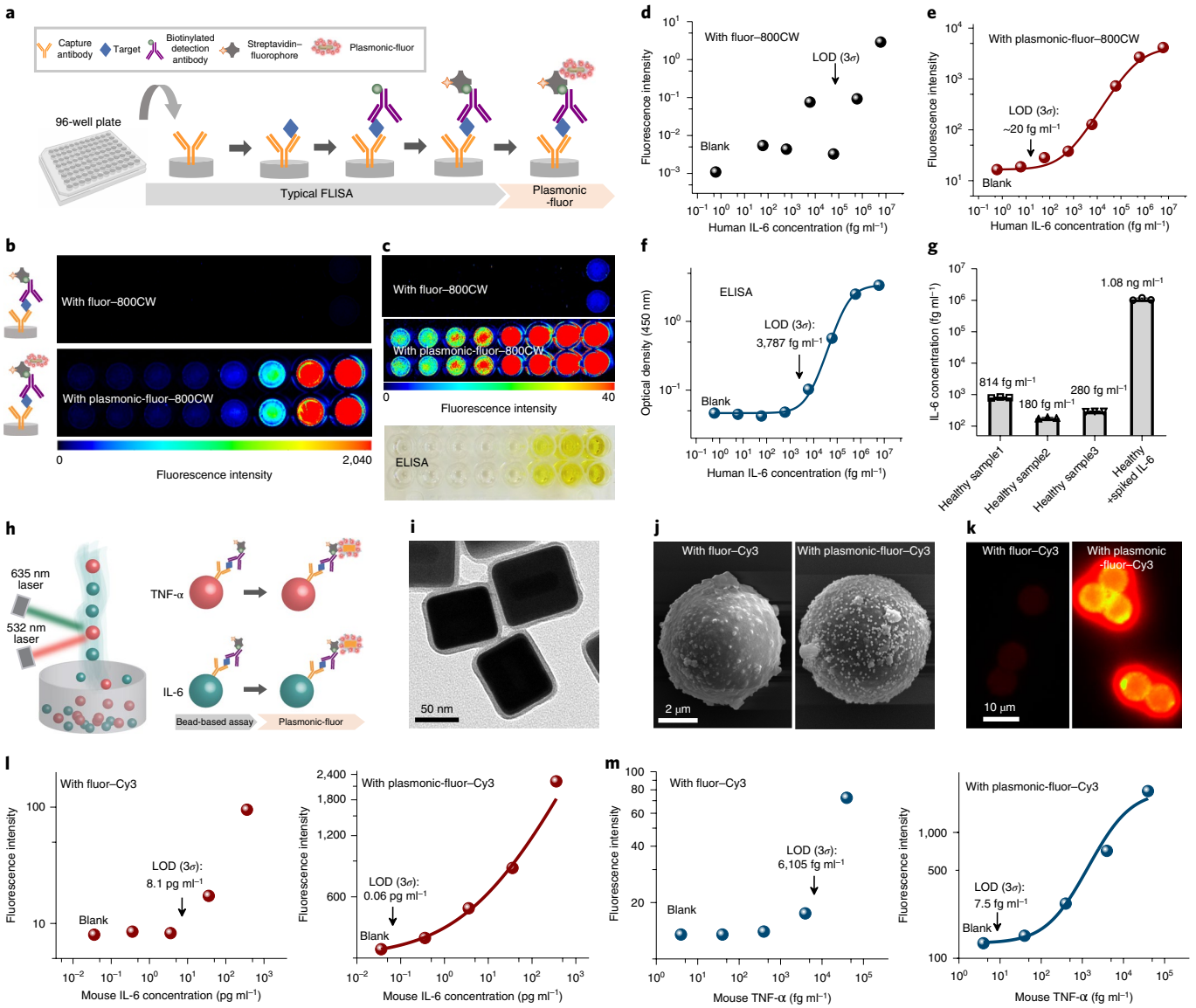

Fig. 3 | p-FLISA and multiplexed bead-based immunoassay. a, Schematic illustration showing the concept of conventional FLISA (800CW) and p-FLISA, implemented in a standard 96-well plate. p-FLISA does not require any change in the routine workflow except adding the plasmonic-fluor as the new, last step. **b**, Fluorescence intensity maps of human IL-6 FLISA and p-FLISA at various analyte concentrations. **c**, Fluorescence intensity maps (with zoomed-in scale bar) of human IL-6 FLISA and p-FLISA and photograph of colorimetric signal of 'gold standard' human IL-6 ELISA. **d**,**e**, Plots showing human IL-6 dose-dependent fluorescence intensity from conventional FLISA (**d**) and p-FLISA (**e**) (each data point represents the average value of duplicate tests, which are included in the Supplementary Information). Compared with conventional FLISA, p-FLISA exhibits 4,750-fold improvement in the LOD and more than three orders of magnitude larger dynamic range. **f**, Plot showing the standard curve of human IL-6 ELISA. Compared with ELISA, p-FLISA exhibited 189-fold lower LOD and more than two orders of magnitude larger dynamic range. **g**, IL-6 concentrations in human serum samples (diluted by tenfold) measured using p-FLISA. Error bars, s.d. ($n = 3$ repeated tests). **h**, Schematic illustration showing the concept of using plasmonic-fluor–Cy3 to enhance the sensitivity of bead-based immunoassay (Luminex assay). **i**, TEM image of plasmonic-fluor–Cy3 utilizing a silver-coated AuNR (AuNR@Ag) as the plasmonic nanoantenna. **j**,**k**, SEM (**j**) and fluorescence (**k**) images of microbead(s) before and after being probed with plasmonic-fluor–Cy3. **l**,**m**, Mouse IL-6 (**l**) and mouse TNF-α (**m**) standard curves obtained before (left) and after (right) applying plasmonic-fluor–Cy3 (each data point represents the average value of duplicate tests, which are included in the Supplementary Information). All fluorescence standard curves are performed independently on different days with different batches of plasmonic-fluors at least three times (data included in the Supplementary Information).

(by more than tenfold) compared with that of the healthy individuals (Supplementary Fig. 17c,d). Moreover, NGAL concentrations determined using 20 min p-FLISA showed a good correlation (linear regression with $R^2 = 0.96$) with those acquired from the standard 280 min ELISA, proving that the accuracy of the ultrafast assay is not compromised (Supplementary Fig. 17e). ELISA, when shortened to 20 min, showed deteriorated performance, and cannot detect urinary NGAL concentrations in several patients or any of the healthy volunteers (Supplementary Fig. 17f).

In addition to the microtitre plate format, we have also investigated the application of plasmonic-fluors as ultrabright reporters in microbead-based multiplexed fluoroimmunoassays, which utilize a non-planar sampling surface. Luminex assay was employed as an example, which utilizes magnetic microbeads embedded with

ratio-set fluorophores as a barcode for each unique analyte (Fig. 3h). The antibody-conjugated microbead captures and facilitates the detection of the analyte in a typical sandwich format and is subsequently probed by streptavidin conjugated with phycoerythrin, a bright fluorescent protein isolated from red algae or cyanobacteria. However, phycoerythrin employed in Luminex assays is structurally unstable and prone to photobleaching[56]. Here, Cy3 (Abcam), a highly stable fluorophore with absorption and emission at 554 nm and 568 nm respectively, similar to phycoerythrin, was employed as a substitute. As discussed above, it is extremely important to choose a plasmonic nanostructure with an LSPR wavelength matching the excitation/emission of the fluorophore[44,57]. To this end, we have employed silver-coated AuNR (AuNR@Ag) nanocuboids with an LSPR wavelength of 520 nm to fabricate plasmonic-fluor–Cy3 (Fig. 3i and Supplementary Fig. 18)[58,59]. Notably, as-synthesized plasmonic-fluor–Cy3 exhibited high brightness and individual nanoconstructs can be easily identified under a common epifluorescence microscope (Supplementary Fig. 19).

We customized the Luminex assay to simultaneously detect mouse IL-6 and mouse tumour necrosis factor-α (TNF-α), which are important pro-inflammatory cytokines involved in cell signalling and immune modulation. The microbeads were incubated with a mixture of serial dilutions of TNF-α and IL-6, followed by the detection antibody cocktail, streptavidin–Cy3 and plasmonic-fluor–Cy3 (Fig. 3h). The beads are subsequently read using a dual laser flow-based instrument (Luminex 200), with the classification laser (635 nm) deciphering the barcode of each bead and the reporter laser (532 nm) determining the intensity of the Cy3 fluorescence, which is in direct proportion to the amount of analyte bound (Fig. 3h). The SEM image of the microbead shows uniform binding of plasmonic-fluor–Cy3 with no sign of aggregation (Fig. 3j). The binding of plasmonic-fluor–Cy3 did not alter the size and shape of the bead (Supplementary Fig. 20) or the optical barcode signal (Supplementary Fig. 21). A substantial increase in the microbead fluorescence intensity was observed after the binding of plasmonic-fluor–Cy3 (Fig. 3k). The LODs of plasmon-enhanced mouse IL-6 and TNF-α assays were determined to be 56.6 fg ml^{-1} (2.7 fM) and 7.5 fg ml^{-1} (0.3 fM), respectively (Fig. 3l,m and Supplementary Fig. 23). Compared with the unenhanced counterpart (Fig. 3l,m and Supplementary Figs. 22 and 23), the plasmon-enhanced assay exhibited 143-fold and 814-fold lower LOD for mouse IL-6 and mouse TNF-α, respectively. Notably, the vendor-specified LOD (using phycoerythrin–streptavidin) for mouse IL-6 (2.3 pg ml^{-1}) and mouse TNF-α (1.47 pg ml^{-1}) were noted to be 41-fold and 196-fold inferior to the plasmon-enhanced Luminex assay. In essence, plasmonic-fluors serve as a powerful technology to enhance the bioanalytical parameters (LOD, LLOQ, dynamic range) of various existing immunoassays without requiring tedious steps or any specialized instruments.

Plasmonic-fluor-enhanced high-throughput multiplexed proteomic array

Biomolecular (micro-)arrays based on fluorescence readout is an important clinical and research tool, especially for simple, high-throughput and rapid proteomic and genetic analysis, allowing miniaturization of thousands of assays on one small piece of analytical substrate[60]. Despite advantages such as high multiplexity, rapid screening and low sample volume, this methodology suffers from low sensitivity (even inferior to ELISA), which hinders its widespread application.

We have investigated the applicability of plasmonic-fluors for enhancing the sensitivity of immunoarrays. An array of antibodies to biomarkers of human kidney disease was employed as a representative example (Fig. 4a). This array is composed of 38 capture antibodies corresponding to human kidney disease protein biomarkers, printed in duplicates on a microporous nitrocellulose membrane (Supplementary Fig. 26). Biotinylated immunoglobulin-G and PBS were printed as a reference positive control and negative control, respectively (Supplementary Fig. 26 and Fig. 4e). A human urine sample from a patient with kidney disease was diluted tenfold using blocking buffer, mixed with biotinylated detection antibody cocktail and added onto the nitrocellulose membrane. After incubation, the membrane was exposed to streptavidin–800CW. Finally, plasmonic-fluor–800CW suspension is added on the array, incubated and thoroughly rinsed to remove the unbound nanoconstructs (Fig. 4a).

SEM images from the positive control region revealed a uniform distribution of plasmonic-fluors on the membrane (including porous subsurface regions) (Fig. 4b). Concurrently, no signal was detected from the negative control (Fig. 4e, blue box) and plasmonic-fluors were not observed in the SEM images from these locations, indicating their minimal non-specific binding (Supplementary Fig. 27). Using conventional fluorophores, out of the 38 target protein biomarkers, only 26 were detectable, most of them exhibiting weak intensity (Fig. 4c,d,f and Supplementary Fig. 28). After addition of the plasmonic-fluor–800CW, the fluorescence signal intensity from each spot of the protein array increased substantially (Fig. 4e,g and Supplementary Fig. 28), enabling the detection and relative quantification of all of the other targets that could not be detected by the conventional fluors (Fig. 4g, [+] mark indicating biomarker detected only with plasmonic-fluors). In addition, we have employed a commercially available 40-plex cytokine microarray as another validation for plasmonic-fluor, where substantial improvement in the microarray sensitivity was observed as well (Supplementary Fig. 31).

It is known that the plasmonic nanostructures at the LSPR wavelength exhibit a large extinction cross-section, which can be up to five to six orders of magnitude larger than light absorption of most organic dyes[61]. This unique property of plasmonic nanostructures renders the possibility of utilizing plasmonic-fluors as a multimodal biolabel[62]. Indeed, the binding of plasmonic-fluor to the sensing domains resulted in analyte concentration-dependent colour spots, which can be directly visualized by the naked eye (Fig. 4h). The colour intensity of each spot in a digital photograph, acquired using a smartphone camera under ambient light condition, was analysed and compared with the corresponding fluorescence intensity (Fig. 4i). We observed a good correlation between the two acquisition modes ($R^2 = 0.86$, Supplementary Fig. 32), which indicates the potential applicability of this nanoconstruct as a 'visible label' in resource-limited settings to alleviate the reliance on a dedicated and expensive readout instrument.

Plasmonic-fluor-enhanced ICC/IF

ICC based on IF is a well-developed semiquantitative method for analysing the relative abundance, conformation and subcellular localization of target antigens in cells. Again, this method lacks the sensitivity to distinguish low-abundance biomolecules from the noise level due to the feeble fluorescence signal of conventional fluorophores. Autofluorescence, the natural emission of light by biological structures, further contributes to the overall low signal-to-noise ratio.

To test the applicability of plasmonic-fluor in ICC/IF, we employed ErbB2 (human epidermal growth factor receptor 2)-positive epithelial breast cancer cells (SK-BR-3) as a model cell line. The surface receptor ErbB2 was immunostained using a standard approach (biotinylated ErbB2 primary antibody and streptavidin–800CW), followed by the addition of plasmonic-fluor–800CW (Fig. 5a). ErbB2 primary antibody (1 mg ml^{-1}) was diluted to different concentrations before incubation with cells. SEM images revealed the uniform distribution of plasmonic-fluors on the cell membrane (Supplementary Fig. 33). Confocal laser scanning microscopy (CLSM) images of the cells revealed up to 100-fold

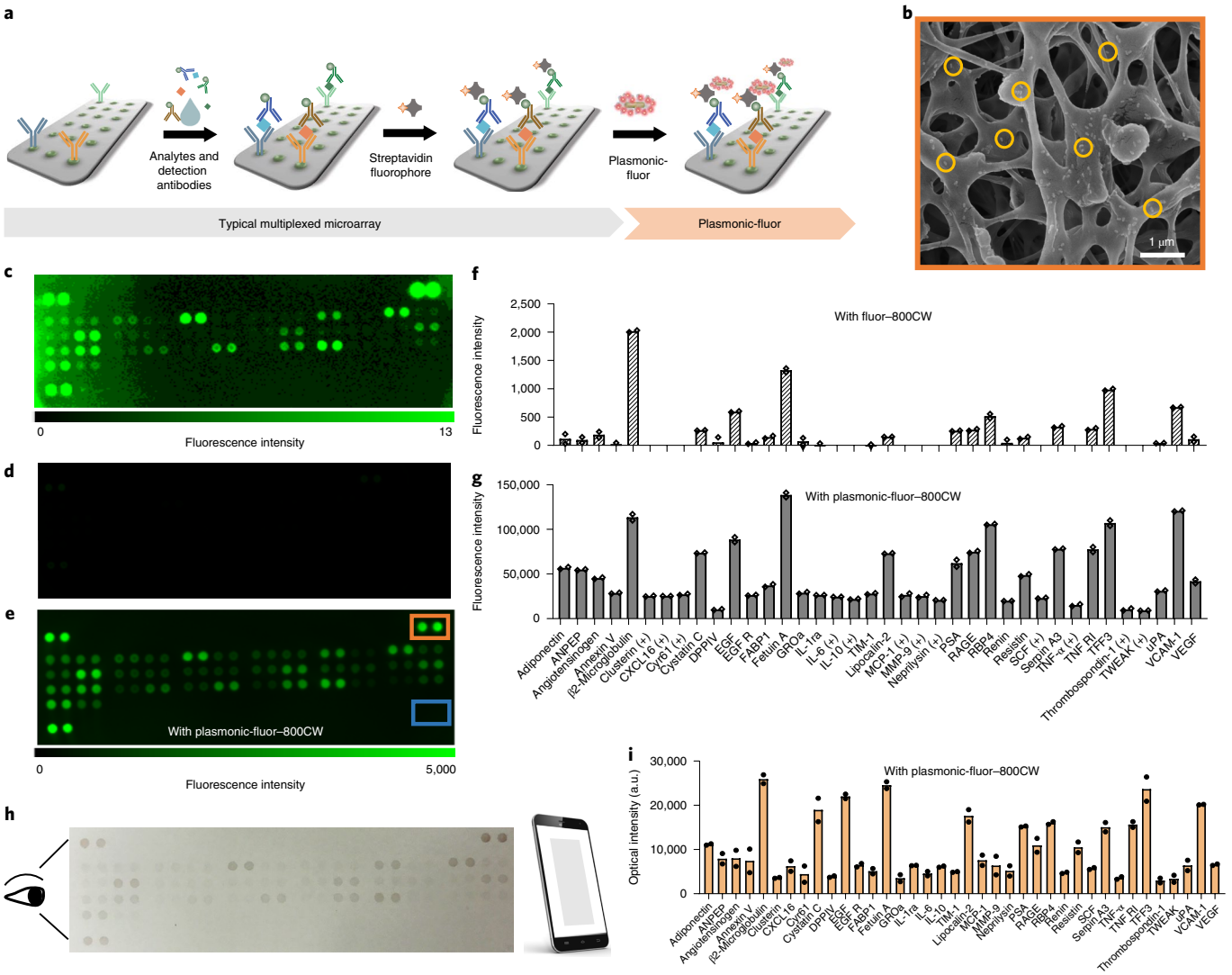

Fig. 4 | Plasmonic-fluor-enhanced high-throughput proteome profiler array. a, Schematic illustration showing the application of plasmonic-fluor–800CW to enhance the bioanalytical parameters of multiplexed proteome profiler for human kidney disease biomarkers implemented on a nitrocellulose membrane. **b**, SEM image showing the uniform distribution of plasmonic-fluor–800CW (a few highlighted by the orange circles) on and in subsurface regions of the nitrocellulose membrane. **c**–**e**, Fluorescence intensity maps showing the kidney disease protein biomarker profile of a patient with kidney disease obtained using conventional fluorophores (streptavidin–800CW; **c**,**d**) and after the addition of plasmonic-fluor–800CW (**e**) (positive and negative controls are highlighted using orange and blue boxes, respectively). Note that (**c**) and (**d**) represent the same image with two different flurorescence intensity scale bars. **f**,**g**, Fluorescence intensity corresponding to the concentrations of various urinary biomarkers before (**f**) (typical assay using conventional fluorophore) and after the addition of plasmonic-fluor–800CW (**g**). (+) indicates biomarkers detected only with plasmonic-fluor–800CW. Experiment was repeated three times independently on different days with different batches of plasmonic-fluors and the data are shown in the Supplementary Information. **h**, Photograph (acquired by mobile phone) showing the colour change of the nitrocellulose membrane with a urine sample from a patient with kidney disease after the addition of plasmonic-fluor–800CW. **i**, Histogram showing the optical intensity of the mobile phone-acquired photograph corresponding to each analyte in the patient urine sample. a.u., arbitrary units.

higher fluorescence signal (background subtracted) after the addition of plasmonic-fluors (20 pM) (Fig. 5a,b and Supplementary Figs. 34 and 35), and the expression of ErBb2 receptors could be imaged even at 100,000-fold dilution of the primary antibody (10 ng ml^{-1}) (Fig. 5a and Supplementary Fig. 34). In stark contrast, the fluorescence signal could only be imaged at a 100-fold (typical dilution; 10 μg ml^{-1}) dilution of primary antibody using conventional fluorophores (Fig. 5a). These results demonstrate not only the applicability of plasmonic-fluor in reducing the amount of antibody (and consequent cost) required in ICC/IF but also the ability to image low-abundance biomarkers on the cell surface using plasmonic-fluors.

Plasmonic-fluor-enhanced flow cytometry

Flow cytometry is extensively employed in cell analysis to measure the expression and relative abundance of specific analytes on or within the cells at rates of thousand or more cells per second (Fig. 5c). However, flow cytometry also suffers from challenges in terms of the fluorescence signal-to-noise ratio due to the high speed of the target species as they cross the laser focus, limiting the time for fluorescence readout[63]. Again, background fluorescence (autofluorescence) from cells poses difficulty in delineating small changes in the expression levels of intra- and extracellular targets.

To test the ability of plasmonic-fluors to enhance the signal-to-noise ratio in flow cytometry-based cell analysis (Fig. 5c),

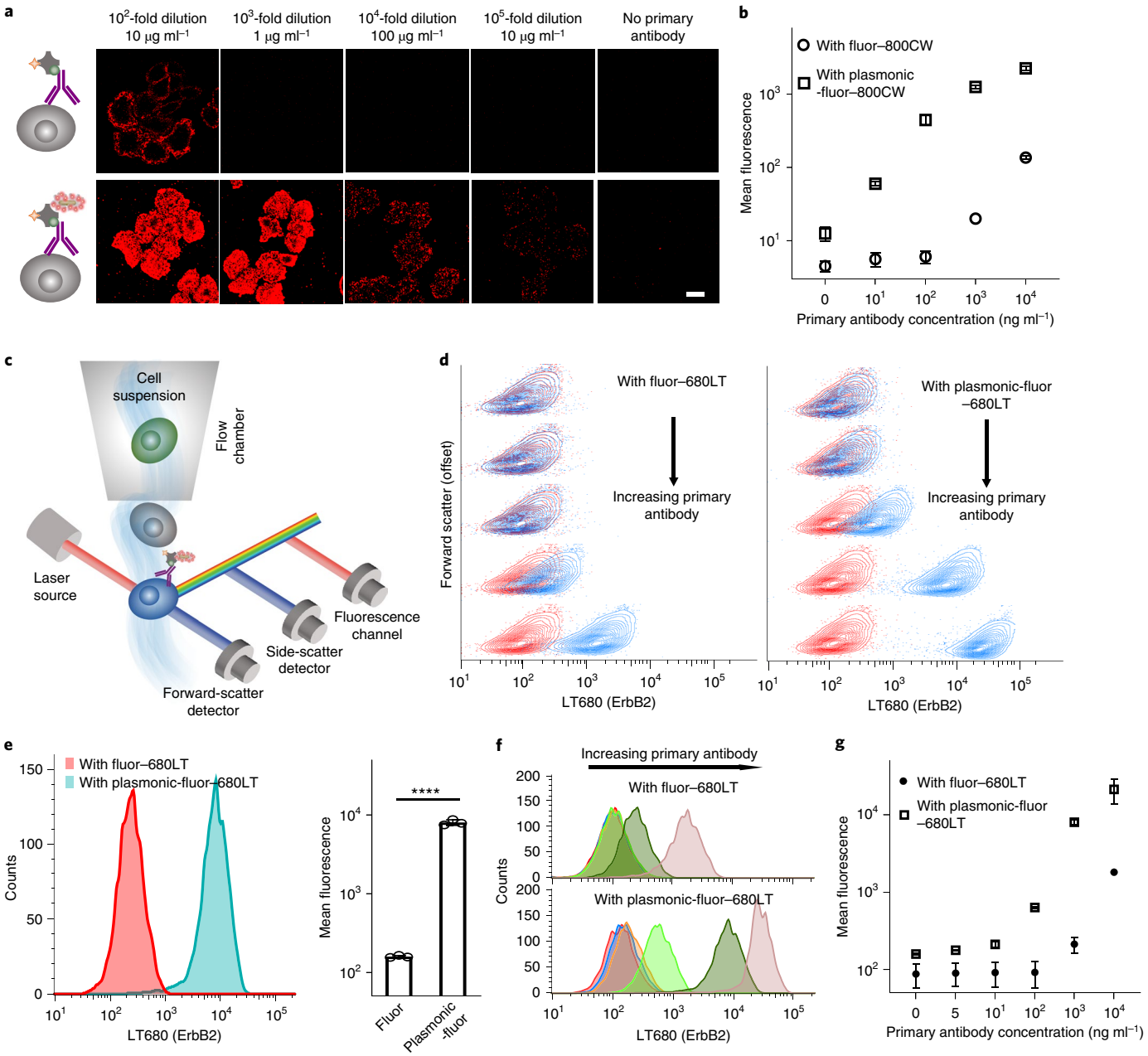

Fig. 5 | Plasmonic-fluor-enhanced ICC and flow cytometry. a, CLSM images of breast cancer cells (SK-BR-3) probed with conventional fluor (800CW, top row) and plasmonic-fluor–800CW (bottom row) at different concentrations of ErbB2 primary antibody. Scale bar, 10 μm. **b**, Plot showing the fluorescence intensity of SK-BR-3 cells stained with conventional fluor and plasmonic-fluor–800CW. Error bars, s.d. (over three different locations). **c**, Schematic illustration showing flow cytometry of ErbB2-stained SK-BR-3 cells probed by conventional fluor (680LT) followed with plasmonic-fluor–680LT. **d**, Flow contour plot (with outliers) of fluorescence versus forward scatter (vertically offset for clarity) of SK-BR-3 cells probed using different concentrations of ErbB2 primary antibody (red, control group without adding primary antibody; blue, cells treated with different dilutions of primary antibody). Cells are stained with conventional fluor (680LT, left) followed by the addition of plasmonic-fluor–680LT (right). **e**, Fluorescence histogram of SK-BR-3 cells probed using conventional fluor (680LT) followed by the addition of plasmonic-fluor–680LT (at 10^3-fold dilution of primary antibody). Error bars, s.d. ($n = 3$ independent tests). $^{****}P < 0.0001$ by two-tailed unpaired *t*-test with Welch's correction. **f**, Histogram showing fluorescence for SK-BR-3 cells before (top) and after (bottom) the addition of plasmonic-fluor–680LT. Red, no primary antibody; blue, 2×10^5-fold dilution; orange, 10^5-fold dilution; light green, 10^4-fold dilution; green, 10^3-fold dilution; rose, 10^2-fold dilution of the stock solution provided by the vendor. **g**, Plot showing the mean fluorescence intensity obtained from flow cytometry at different primary antibody concentrations. Error bars, s.d. ($n = 3$ independent tests). All experiments were repeated three times independently on different days with different batches of plasmonic-fluors and the data are shown in the Supplementary Information.

SK-BR-3 cell suspensions were incubated with ErbB2 primary antibody, streptavidin 680LT (LI-COR), followed by the addition of plasmonic-fluor–680LT. Subsequently, the labelled cells were collected by mild centrifugation (1,000 r.p.m.) with concomitant removal of unbound plasmonic-fluors. To match the excitation laser and fluorophore emission, we have employed AuNRs with an LSPR wavelength of around 647 nm as the nanoantennae to create plasmonic-fluor–680LT (Supplementary Fig. 38). Specific binding of

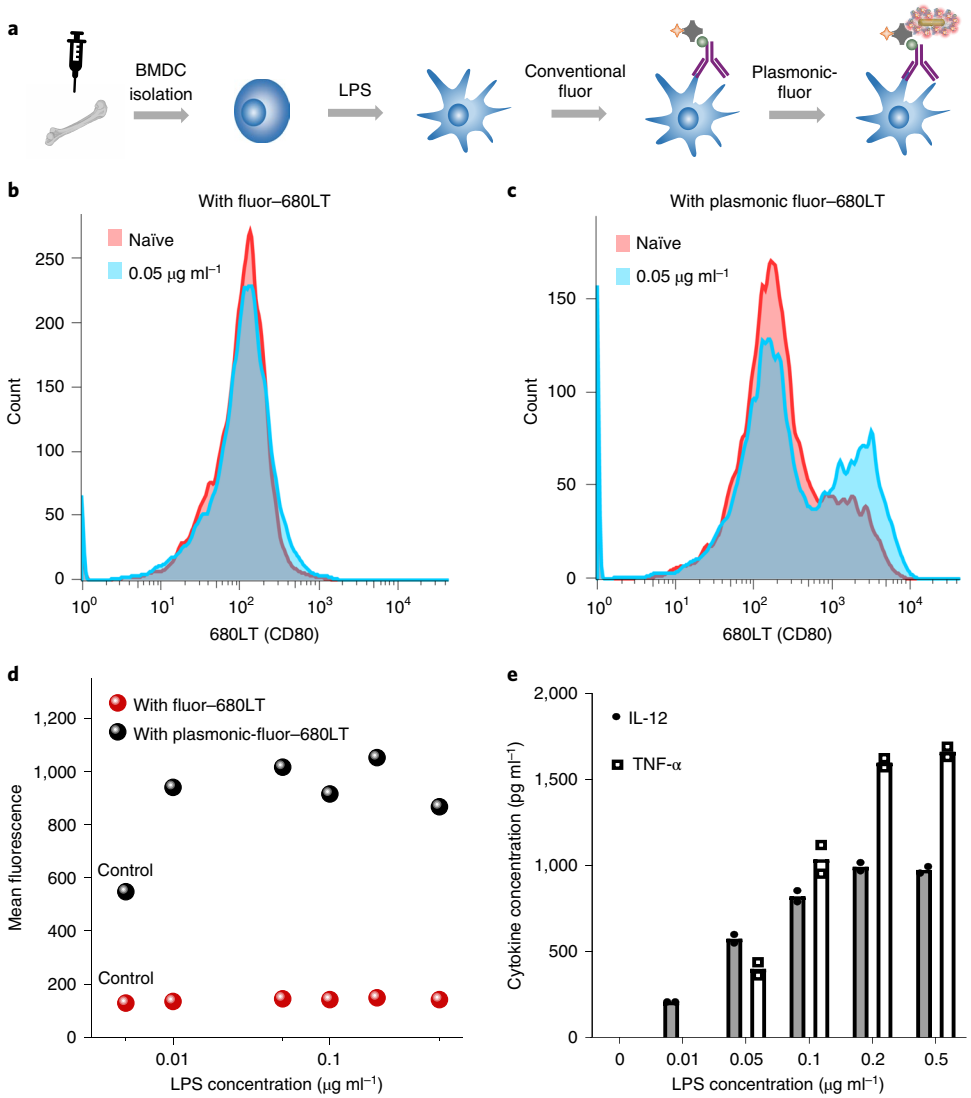

Fig. 6 | Flow cytometry analysis of BMDC maturation maker probed by conventional fluor (680LT) and plasmonic-fluor–680LT. a, Schematic illustration showing BMDCs treated with the immunostimulant (LPS). The small changes of maturation markers (CD80) expression after stimulation are detected by IF staining followed by addition of plasmonic-fluor–680LT. **b**,**c**, Fluorescence intensity distribution corresponding to naïve (control) and LPS-stimulated BMDCs obtained using conventional fluors (680LT) (**b**) and plasmonic-fluor–680LT (**c**). **d**, Plot showing mean fluorescence intensity of BMDCs (corresponding to the expression level of CD80) after stimulation with different amounts of LPS. The experiment was repeated three times independently on different days with different batches of plasmonic-fluors and the data are shown in the Supplementary Information. **e**, Secretion levels of pro-inflammatory cytokines (TNF-α and IL-12), which confirmed the dose-dependent activation and maturation of BMDCs. Each data point represents the average value of duplicate tests, which are included in the Supplementary Information.

the plasmonic-fluor–680LT caused a change in the colour of the cell pellet (Supplementary Fig. 39). The presence of plasmonic-fluors–680LT on the cell surface did not change the forward-scatter or side-scatter intensity (Supplementary Fig. 40), indicating that the cell size and granularity/complexity remained virtually unaltered after binding of the plasmonic-fluor–680LT. Flow cytogram of fluorescence versus forward scatter (vertically offset for clarity) of SK-BR-3 cells revealed a more obvious separation of cell populations stained with plasmonic-fluor–680LT compared with that obtained with conventional fluorophores (Fig. 5d). Histograms of cell fluorescence signals revealed up to 60-fold higher intensity (background subtracted) using plasmonic-fluor–680LT compared with its conventional counterpart (Fig. 5e). Fluorescence histogram revealed that the expression of ErbB2 on the cell surface can be detected even at 200,000-fold dilution of primary antibody (5 ng ml^{-1}) using plasmonic-fluor–680LT labelling (Fig. 5f,g). However, conventional labelling required the antibody to be diluted less than 1,000-fold (that is, concentration >0.5 μg ml^{-1}) to ensure a detectable increase in fluorescence signal compared with the background (blank) (Fig. 5f,g).

To further validate the performance of plasmonic-fluors in delineating cell populations with small differences in surface receptor expression levels, we employed bone marrow-derived dendritic cells (BMDCs) as a model system in which the surface expression of receptors can be modulated using immunogenic stimulus. Dendritic cells after exposure to an immunogenic stimulus undergo activation and maturation, which leads to cytokine secretion and upregulation of maturation markers such as cluster of differentiation 40 (CD40), CD80, CD86 and major histocompatibility complexes (MHC I and MHC II). Here, BMDCs were isolated from 6- to 8-week-old C57BL/6 mice and LPS was employed as immunogenic stimulus to trigger the upregulation of CD80 and cytokine release in a dose-dependent manner. Subsequently, the cells were fixed

and treated with biotinylated CD80 antibody. Finally, BMDCs were probed by conventional fluorophore (680LT, LI-COR) followed by plasmonic-fluor–680LT, and the fluorescence levels were compared using a flow cytometer (Fig. 6a).

Figure 6b,c shows the fluorescence histograms corresponding to naïve and LPS (0.05 μg ml^{-1})-stimulated BMDCs obtained using conventional fluors (680LT, Fig. 6b) and plasmonic-fluor–680LT (Fig. 6c). Clearly, plasmonic-fluor-stained BMDCs exhibited a substantial fluorescence difference between activated (blue) and naïve (red) cell populations (Fig. 6b,c and Supplementary Fig. 43). LPS dose-dependent (0 to 0.05 μg ml^{-1}) stimulation of BMDCs was further investigated, where a steep increase in the mean fluorescence intensity was observed using plasmonic-fluor–680LT followed by a plateau at higher LPS doses (Fig. 6d and Supplementary Fig. 44), indicating an increase in the expression of CD80. BMDCs stained with conventional fluorophore, however, exhibited a shallow fluorescence increase with LPS dose, which was obscured by the high fluorescence background (Fig. 6d and Supplementary Fig. 44). Moreover, the secretion levels of pro-inflammatory cytokines (TNF-α and IL-12) exhibited an increasing trend with increasing LPS concentration (Fig. 6e and Supplementary Fig. 45). This further confirmed the dose-dependent activation and maturation of BMDCs as well as the specificity and accuracy of plasmonic-fluor in differentiating the minute changes in the cell-surface maturation markers.

Harnessing plasmon-enhanced fluorescence, we have designed and synthesized ultrabright nanoconstructs as a fluorescence reporter. In addition to the improved bioanalytical parameters, plasmonic-fluors can potentially simplify the readout instrumentation, decrease the required sample volume, shorten the overall assay time and enable bioassays to be implemented with minimal effort and reduced cost. Through a series of experiments, we have demonstrated that plasmonic-fluors are highly customizable in terms of the excitation/emission wavelength over the entire visible and NIR range and can be applied in microtitre plates, on porous membranes, on microbeads and cells. The cross-assay signal amplification approach introduced here is a disease-, biomarker- and application-agnostic ubiquitously applicable fundamental and enabling biomedical technology to immediately improve the sensitivity of existing bioanalytical methodologies in an easy-to-implement and cost-effective manner.

Methods

Synthesis of AuNRs. AuNR-760 (LSPR wavelength ~760 nm) was prepared by a seed-mediated method[64,65]. An Au seed was synthesized by adding 0.6 ml of ice-cold $NaBH_4$ solution (10 mM) (Sigma-Aldrich, 71321) into a solution containing 0.25 ml of $HAuCl_4$ (10 mM) (Sigma-Aldrich, 520918) and 9.75 ml of CTAB (0.1 M) (Sigma-Aldrich, H5882) under vigorous stirring at room temperature. The colour of the solution changed from yellow to brown indicating the formation of Au seed. For the synthesis of AuNR, the growth solution was prepared by the sequential addition of aqueous $HAuCl_4$ (0.01 M, 2 ml), CTAB (0.1 M, 38 ml), $AgNO_3$ (0.01 M, 0.5 ml, Sigma-Aldrich, 204390), HCl (1 M, 0.8 ml, Sigma-Aldrich, H9892) and ascorbic acid (0.1 M, 0.22 ml, Sigma-Aldrich, A92902) followed by gentle inversion to homogenize the solution. The $AgNO_3$ and HCl volume ratio may slightly vary to obtain the right LSPR wavelength. Subsequently, 5 μl of the seed solution was added into the growth solution and left undisturbed in the dark for 24 h. The AuNR solution was centrifuged at 7,000 r.p.m. for 40 min to remove the supernatant and the AuNR was re-dispersed into nanopure water to achieve a final peak extinction of ~2.0. For AuNR-647 (LSPR wavelength ~647 nm), the growth solution contained $HAuCl_4$ (0.01 M, 2 ml), CTAB (0.1 M, 38 ml), $AgNO_3$ (0.01 M, 0.2 ml, this value may slightly vary) and ascorbic acid (0.1 M, 0.32 ml).

Synthesis of AuNR@Ag. The AuNR with an LSPR wavelength around 711 nm was employed as the core for the synthesis of AuNR@Ag nanostructures. Specifically, 3 ml of AuNR (peak extinction ~4) was incubated with 8 ml of CTAC (20 mM) at 60 °C for 20 min under stirring. Then, 8 ml of $AgNO_3$ (4 mM), 4 ml of CTAC (20 mM) and 0.8 ml of ascorbic acid (0.1 M) were added sequentially and the mixture was incubated at 60 °C for 4 h under magnetic stirring to form AuNR@Ag nanocuboids. Finally, AuNR@Ag nanocuboids solution was centrifuged at 6,000 r.p.m. and the nanocuboids were re-dispersed in nanopure water.

Conjugation of biotin and 800CW on BSA. Biotin and 800CW were sequentially conjugated to BSA through EDC (1-ethyl-3-(3-dimethylaminopropyl) carbodiimide)/NHS (N-hydroxysuccinimide) chemistry. In pH 7–9 buffers, NHS esters react efficiently with primary amino groups ($-NH_2$) by nucleophilic attack, forming an amide bond and releasing the NHS. Specifically, 2 mg of NHS activated biotin (NHS-PEG4-biotin, Thermo Scientific, product number 21329) was added to 2.2 ml of BSA (Sigma-Aldrich, A7030) solution (5 mg ml^{-1} in 1X PBS). The mixture was incubated at room temperate (~22 °C) for 1 h to complete the reaction. Excess NHS-PEG4-biotin was removed from the solution using a desalting column (5 ml, 7,000 MWCO, Thermo Scientific, product number 21329) pre-equilibrated with 1X PBS. Next, 800CW was conjugated to BSA–biotin. We added 0.1 ml of 1 M potassium phosphate buffer (K_2HPO_4, pH 9) into 1 ml of purified BSA–biotin solution to raise the pH. Next, 25 μl of 4 mg ml^{-1} NHS-800CW (LI-COR, 929-70020) was added to the mixture and the solution was incubated at 23 °C for 2.5 h. Free NHS-800CW was then separated from the conjugate using a Zeba desalting column pre-equilibrated with nanopure water. BSA–biotin–680LT and BSA–biotin–Cy3 were prepared using a similar method, except for changing the fluorophore to NHS-680LT (LI-COR, 929-70010) and NHS-Cy3 (ab146452).

Synthesis of plasmonic-fluor. To synthesize plasmonic-fluor with high brightness, it is extremely important to choose an 'on-resonant' plasmonic nanostructure for a given fluorophore. For 800CW, AuNR-760 (length and diameter of 83 and 24 nm, respectively) was employed as the nanoantenna. One microlitre of MPTMS (Sigma-Aldrich, 175617) was added to 1 ml AuNR with extinction of ~2.0 and the mixture was shaken for 1 h allowing the formation of an interfacial layer on the AuNR. The MPTMS-modified AuNR was further mixed with different volumes of APTMS (Sigma-Aldrich, 281778) and TMPS (Sigma-Aldrich, 662275) (from 0.5 μl to 2 μl) to form the polymer spacer layer on the AuNR. Finally, the AuNR/polymer solution was centrifuged twice each at 6,000 r.p.m. for 10 min to remove the free monomer. After second centrifugation, the AuNR/polymer was concentrated into a final volume of 10 μl.

Next, the BSA–biotin–800CW conjugate was coated around the AuNR/polymer. We have adopted a previously reported method to coat the BSA around the metal nanostructures with a few modifications[66]. Specifically, 1 μl of 20 mg ml^{-1} citric acid (Alfa Aesar, 36664) was added into 100 μl of BSA–biotin–800CW (~4 mg ml^{-1}) to lower the pH. The concentrated AuNR/polymer solution was subsequently added into this mixture and sonicated for 20 min under dark conditions. The nanostructures were then collected using mild centrifugation (5,000 r.p.m. for 3 min). Subsequently, the AuNRs were incubated with 0.5 ml BSA–biotin–800CW (~0.4 mg ml^{-1}, pH = 10) for 3 d under dark conditions at 4 °C. Finally, the nanostructures were washed four times using nanopure water (pH 10) by centrifugation at 6,000 r.p.m. After the last washing step, the particles were re-dispersed into 1% BSA (buffered with 1X PBS).

Material characterization. TEM images were obtained using a JEOL JEM-2100F field emission instrument. A drop of aqueous solution was dried on a carbon-coated grid, which had been made hydrophilic by glow discharge. SEM images were obtained using a FEI Nova 2300 field-emission scanning electron microscope at an acceleration voltage of 10 kV. AFM imaging was performed on a Dimension 3000 using silicon cantilevers with a nominal spring constant of 40 N m^{-1} in light tapping mode. The extinction spectra of plasmonic nanostructures were obtained using a Shimadzu UV-1800 spectrophotometer. Fluorescence lifetime was measured using time-correlated single-photon counting (TCSPC implemented in Fluorolog-3, Horiba Jobin Yvon) with a 740 nm excitation source NanoLed (impulse repetition rate 1 MHz) at 90° to the PMT R928P detector (Hamamatsu Photonics). Most of the fluorescence mappings were recorded using LI-COR Odyssey CLx imaging system. Luminex 200 system was employed to read the fluorescence signal from the microbeads. Cell imaging was performed using Olympus FV1000 LSM confocal laser scanning microscopy (785 nm excitation laser) under ×40 water-immersion objective. Guava easyCyte was employed to acquire the flow cytometry data.

Fluorescence enhancement of 800CW–streptavidin using AuNR–plasmonic-fluor–800CW and AuNP–plasmonic-fluor–800CW. The experimental procedure employed for this test is illustrated in Supplementary Fig. 9 and the data are shown in Fig. 2c,d. Specifically, BSA–biotin was first immobilized on the bottom of plastic 96-well plate by incubating the well with 50 ng ml^{-1} of BSA–biotin (in 1X PBS) at room temperature for 15 min. The plate was washed three times using PBST (0.05% Tween 20 in 1X PBS) and then blocked using Odyssey Blocking Buffer (PBS) (LI-COR, P/N 927-40100). Wells coated with BSA–biotin were subsequently incubated with 1 μg ml^{-1} of streptavidin–800CW (in Odyssey Blocking Buffer) for 10 min to allow specific binding of streptavidin to biotin. Next, the plate was washed three times using PBST and then incubated with ~76 pM plasmonic-fluor–800CW (in 1% BSA). The plate was washed three more times using PBST to remove free plasmonic-fluor. Finally, 200 μl of PBST was added into each well and the fluorescence signal before and after the addition of plasmonic-fluor was recorded using the LI-COR CLx fluorescence imager with the following scanning parameters: laser power ~L2; resolution ~169 μm; channel 800; height 4 mm. The experiment was repeated four times independently and the fluorescence intensities before and after adding plasmonic-fluor–800CW were compared. The data are statistically significant, and the P value was calculated to be 0.0044, $^{**}P < 0.01$ by two-tailed unpaired t-test with Welch's correction.

To compare the fluorescence enhancement efficiency of plasmonic-fluor–800CW composed of AuNR and AuNP, similar experiment was performed except using AuNP–plasmonic-fluor–800CW instead of AuNR–plasmonic-fluor–800CW after the binding step of streptavidin–800CW. The molar concentration of AuNP–plasmonic-fluor–800CW was maintained to be similar as that of AuNR. The experiment was repeated three times independently. The fluorescence enhancement factor obtained from AuNP–plasmonic-fluor–800CW was compared with that obtained from AuNR–plasmonic-fluor–800CW. Data are statistically significant with P value = 0.0013, $^{**}P < 0.01$ by two-tailed unpaired t-test with Welch's correction.

Human IL-6 ELISA. Human IL-6 DuoSet ELISA kit (R&D, catalogue number DY206, lot number P173353) was employed in the study. Specifically, 96-well plates were first coated with capture antibodies (2 μg ml^{-1} in PBS, part number 840113) through overnight incubation at room temperature, followed by blocking with 300 μl of reagent diluent (1X PBS containing 3% BSA, 0.2 μm filtered). After three times washing with PBST, 100 μl of serial diluted standard samples (part number 840115) as well as patients' serum samples (tenfold dilution using reagent diluent) were added into different wells and the plate was incubated at room temperature for 2 h. The plate was washed subsequently and incubated with biotinylated detection antibodies (part number 840114, 50 ng ml^{-1} in reagent diluent) for 2 h, washed again with PBST and incubated with HRP (horseradish peroxidase)-labelled streptavidin (part number 893975, 200-fold dilution using reagent diluent) for 20 mins. One-hundred microlitres of substrate solution (1:1 mixture of Colour Reagent A (H_2O_2) and Colour Reagent B (tetramethylbenzidine) (R&D Systems, catalogue number DY999)) was added to each well and the reaction was stopped by adding 50 μl of H_2SO_4 (2N) (R&D Systems, catalogue number DY994) after 20 min. The optical density of each well was determined immediately using a microplate reader set to 450 nm.

Human IL-6 FLISA and p-FLISA. Human IL-6 FLISA was implemented adopting the similar approach as the ELISA described above, expect that HRP-labelled streptavidin was replaced by 800CW-labelled streptavidin (LI-COR P/N 926-32230, 50 ng ml^{-1} for 20 min). The plate was washed three times using PBST followed by washing with nanopure water. In p-FLISA, plasmonic-fluor–800CW was added subsequently (extinction ~1, 100 μl), incubated for 30 min, and the plate was washed three times each with reagent diluent followed by PBST. The plate was imaged using LI-COR CLx fluorescence imager with the following scanning parameters: laser power ~L2; resolution ~169 μm; channel 800; height 4 mm. The results from independent experiment are shown in the main manuscript (Fig. 3d,e) as well as in Supplementary Fig. 13.

Human NAGL ELISA (280 min) and p-FLISA (20 min). Human NGAL DuoSet ELISA kit (R&D, catalogue number DY1757, lot number P195696) was employed in the study. Specifically, 100 μl of serial diluted standard samples (part number 842273) as well as urinary samples from patients and self-described healthy volunteers (tenfold dilution using reagent diluent) were added into different wells and the plate was incubated at room temperature for 2 h. The plate was washed subsequently and incubated with biotinylated detection antibodies (part number 844865, 25 ng ml^{-1} in reagent diluent) for 2 h, washed again with PBST and incubated with HRP-labelled streptavidin (part number 893975, 40-fold dilution using reagent diluent) for 20 min. Human NGAL p-FLISA was performed by adopting a similar procedure as the ELISA with a shortened assay time. Specifically, the incubation time for standards/samples, biotinylated detection antibodies, 800CW-labelled streptavidin (LI-COR P/N 926-32230, 50 ng ml^{-1}) and plasmonic-fluor–800CW (extinction ~1, 100 μl) was set to 5 min. The study was approved by Washington University institutional review board (IRB) 201601082 'Nanotech Biomarkers for Renal Cancer Intervention: Clinical Validation and Utility' and IRB 201202051 'Urine Proteome of Surgical Patients and Healthy Volunteers'. Informed consent was obtained from the participants.

Measurement of mouse IL-6 concentration in dermal ISF. C57BL/6J female mice (nine to ten weeks of age) were intraperitoneally injected with LPS (1 μg g^{-1}) to induce an acute phase response and systemic inflammation. Mouse ISF was collected 4 h after LPS injection and the concentration of pro-inflammation cytokine (IL-6) in ISF was analysed by ELISA and p-FLISA. Mouse ISF was extracted according to previously reported centrifugation method[67]. Briefly, the skin on the back of the mice was collected and placed on a basket of nylon mesh with pore size ~15–20 μm, with the subcutis facing the mesh. The skin sample was subsequently transferred to a centrifuge tube and was immediately spun at 424 g at 4 °C to collect the ISF. ISF samples from naïve mice without any immune stimulation were collected using the same method.

Mouse IL-6 DuoSet ELISA kit (R&D, catalogue number DY406-05, lot number P195781) was employed to measure the IL-6 concentration in mouse ISF. Specifically, 100 μl of serial diluted standards (part number 840173) as well as diluted ISF samples were added into different wells and the plate was incubated at room temperature for 3 h. The plate was washed subsequently and incubated with biotinylated detection antibodies (part number 840172, 75 ng ml^{-1} in reagent diluent) for 2 h, washed again with PBST and incubated with HRP-labelled streptavidin (part number 893975, 40-fold dilution using reagent diluent) for 20 min. Mouse IL-6 p-FLISA was performed by adopting a similar approach as the ELISA described above, expect that HRP-labelled streptavidin was replaced by 800CW-labelled streptavidin (LI-COR P/N 926-32230, 20 ng ml^{-1} for 20 min). Finally, plasmonic-fluor–800CW (extinction ~0.5, 100 μl) was added, incubated for 30 min and washed by PBST.

Plasmonic-fluor-enhanced Luminex bead-based assay. Mouse magnetic Luminex assay was purchased from R&D systems (catalogue number LXSAMSM-03, lot number L126064), which was customized to simultaneously detect mouse TNF-α and mouse IL-6. To begin with, 50 μl of standards that contain different concentrations of TNF-α and IL-6 (part number 984658) were mixed with 50 μl of diluted microbead cocktail (part number 894724) in a 96-well plate. The mixture was homogenized by shaking horizontally using a microplate orbital shaker (0.12″ orbit) set at 800 r.p.m. for 2 h. Microbeads were subsequently collected using a magnetic device (Millipore Sigma 40–285) designed to accommodate the microplate and were washed by removing the liquid and filling with wash buffer (part number 895003). The washing step was repeated by three times. Next, 50 μl of diluted biotin-antibody cocktail (part number 894666) was introduced to each well and incubated for 1 h on the shaker at 800 r.p.m. The microbeads were washed three times again and then incubated with 100 ng ml^{-1} Cy3–streptavidin (in 3% BSA buffered with 1X PBS) for 30 min at 800 r.p.m. After three washes, the microbeads were incubated with 50 μl plasmonic-fluor–Cy3 (extinction ~5, 100 μl) for 1 h at 800 r.p.m and washed three times each with 3% BSA and washing buffer. Finally, the microbeads were resuspended in 100 μl washing buffer and incubated for 2 min at 800 r.p.m. before reading. A Luminex 200 instrument was employed for fluorescence readout. Dual mode fluorescence of the microbead was observed on a Confocor II LSM system (Carl Zeiss-Evotec) using a ×40 water-immersion objective. The results from independent experiment are shown in the main manuscript (Fig. 3l,m) as well as in Supplementary Figs. 24 and 25.

Plasmonic-fluor-enhanced human kidney biomarker array. A human kidney biomarker array kit was purchased from R&D system (catalogue number ARY019, lot number 1311110). A urine sample from a patient with kidney disease (ID number 25, age 61, male) was employed for this study. The study was approved by Washington University IRB 201601082 'Nanotech Biomarkers for Renal Cancer Intervention: Clinical Validation and Utility'. Informed consent was obtained from the participants. The nitrocellulose membrane (part number 893967) was blocked by incubation with 2 ml of blocking buffer (part number 893573) in the four-well multidish for 1.5 h under gentle rocking. During the blocking process, the patient with kidney disease (ID number 25) urine sample (150 μl) was diluted with 500 μl of blocking buffer and 850 μl of array buffer (part number 895876), resulting in a total tenfold dilution. The diluted urine sample was mixed with 15 μl of reconstituted detection antibody cocktail (part number 893966) and the mixture was incubated at room temperature for 1 h. The nitrocellulose membrane was taken out from the blocking solution and incubated with the mixture of urinary sample and biotinylated detection antibodies for overnight at 4 °C. The membrane was subsequently washed with 20 ml of 1X washing buffer (part number 895003) for 10 min under gentle rocking, and the washing process was repeated two more times. Next, the membrane was incubated with 800CW–streptavidin (50 ng ml^{-1} in 1% BSA) for 30 min under gentle rocking, washed three times and incubated with plasmonic-fluor–800CW (extinction ~0.5, 2 ml) for one more hour. Finally, the membrane was imaged using the LI-COR CLx imager at L2 laser power, with focusing height at 0.5 mm and resolution of 169 μm. The photograph of the protein array was acquired using the iPhone6 camera and the image was analysed using Image Studio Lite software to measure the median intensity of each spot (background subtracted). The results from independent experiments are shown in the main manuscript (Fig. 4f,g) as well as in Supplementary Figs. 29 and 30.

Plasmonic-fluor-enhanced human cytokine microarray. Forty-plex human cytokine microarray (RayBiotech, catalogue number QAH-CYT-4) was employed to further test the efficacy of plasmonic-fluor. First, the glass substrate of the microarray was blocked with 100 μl of sample diluent (catalogue number QA-SDB) followed by incubation with sample standard (catalogue number QAH-CYT-4-STD) at room temperature for 2 h with gentle rocking. The microarray was washed five times using 1X wash buffer I (catalogue number AA-WB1-30ML) followed by two washes with 1X wash buffer II (catalogue number AA-WB2-30ML). Next, 80 μl of reconstituted detection antibody cocktail was added into each well and incubated for another 2 h under gentle rocking. Following the incubation, the washing process was repeated again as described above. Subsequently, 80 μl of 800CW–streptavidin (50 ng ml^{-1} in 1% BSA) was added to the array slide and incubated for 20 min, washed and immersed with plasmonic-fluor–800CW (extinction ~1, 100 μl) for 1 h. The slide was scanned using LI-COR CLx scanner with the following parameters: laser power ~3.5; resolution ~21 μm; channel 800; height 1.8 mm.

Plasmonic-fluor-enhanced ICC/IF. Human epithelial breast cancer cells SK-BR-3 (SKBR3) (ATCC HTB30) were purchased from ATCC and subcultured in Mc.Coy's 5A medium with 10% fetal bovine serum and antibiotics (100 μg ml^{-1} of penicillin and 100 μg ml^{-1} of treptomycin) (Sigma). Cells were cultured in water

jacketed incubator at 37 °C with 5% CO_2-humidified atmosphere in T-25 tissue culture flasks. Once the cells reached to 90% confluence, they were washed with PBS and detached from the flask bottom using a scraper. After centrifugation, cells were re-dispersed in culture medium and seeded on six-well plate for overnight to allow attachment to the plate bottom. Cells were subsequently fixed using 3.7% formaldehyde (in 1X PBS) for 30 min, washed three times with 1X PBS and blocked with 3% BSA for 1 h. Next, ErbB2 primary antibody (anti-human HER-2/biotin, eBioscience, clone 2G11, reference number BMS120BT, lot number 186281000) was diluted using 1% BSA and incubated with SK-BR-3 cells for 1.5 h. The cells were subsequently washed three times, incubated with 800CW–streptavidin (1 μg ml^{-1} in 1% BSA) for 30 min, washed for another three times and probed with plasmonic-fluor–800CW (extinction ~0.3, 2 ml). The cells were finally imaged using Olympus FV1000 LSM confocal laser scanning microscopy (785 nm excitation laser) under ×40 water-immersion objective. The results from independent experiment are shown in the main manuscript (Fig. 5a) as well as in Supplementary Figs. 36 and 37.

SK-BR-3 flow cytometry. SK-BR-3 cells were cultured and collected using the method described above. The cells were centrifuged at 1,000 r.p.m. for 10 min to remove the culture medium and were subsequently fixed using 3.7% formaldehyde in 1X PBS for 30 min. The cell suspension was centrifuged again to remove the free formaldehyde and the cells were subsequently blocked with 3% BSA for overnight. Next, different amounts of ErbB2 primary antibody were added into the cell suspension and the mixture was incubated for 1 h under gentle shaking. The cells were centrifuged at 1,000 r.p.m. and washed once with 1X PBS to remove the free antibody, incubated with streptavidin 680LT (LI-COR: P/N 926-6803; 1 μg ml^{-1} in 1% BSA) for 1 h, washed two more times and incubated with plasmonic-fluor–680LT (extinction ~2.0, 200 μl) for 1 h. Finally, 5,000 cells were analysed by Guava easyCyte to acquire the fluorescence signal (RED-R channel (excitation laser 642 nm; filter 662/15 nm)) in combination with forward scatter and side scatter. The results from independent experiment are shown in the main manuscript (Fig. 5f,g) as well as in Supplementary Figs. 41 and 42.

BMDC isolation and flow cytometry. Female C57BL/6 (H-2b) mice that were five to six weeks of age were purchased from Jackson Labs. The mice were maintained under pathogen-free conditions. All experiments employing mice were performed in accordance with laboratory animal protocol approved by the School of Medicine Animal Studies Committee of Washington University in St. Louis. Mice were euthanized using CO_2 asphyxiation and cervical dislocation. The euthanized mice were kept in 70% (v/v) ethanol for 1 min. Both the femurs and tibiae were isolated, and the muscle attachments were carefully removed using gauze pads. Both ends of the bones were cut with scissors and the marrow was centrifuged in an adapted centrifuge tube (0.6 ml tube with a hole inserted in 1.5 ml tube) at 1,000 r.p.m. for 10 s. The pellet was resuspended by vigorous pipetting in RPMI 1640 media. The cells were passed through a 70 μm cell strainer to prepare a single-cell suspension. After one wash (1,200 r.p.m., 5 min), red blood cells were depleted with RBC lysis buffer (Sigma-Aldrich). The bone marrow cells were collected and cultured in 100 mm Petri dishes containing 10 ml of RPMI medium supplemented with 10% heat-inactivated fetal bovine serum, 50 IU ml^{-1} of penicillin, 50 μg ml^{-1} of streptomycin and 20 ng ml^{-1} of mouse recombinant granulocyte-macrophage colony-stimulating factor (R&D Systems). BMDCs (1×10^6) were cultured in six-well plates and were stimulated by adding 1 ml of different concentrations of LPS (0.5, 0.2, 0.1, 0.05, 0.01 and 0 μg ml^{-1}) for 24 h. Cells were collected using a cell scraper for further staining and flow cytometry analysis.

CD80 overexpressed on the cell surface was probed using conventional fluorophore followed with plasmonic-fluor–680LT. Specifically, stimulated BMDCs were washed once with 1X PBS to remove the culture medium (centrifugation at 2,000 r.p.m. for 5 min) and fixed using 10% neutral buffered formalin for 20 min. The cells were then washed (2,000 r.p.m. for 5 min) and blocked with 3% BSA for overnight at 4 °C. Next, biotinylated CD80 primary antibody (anti-Mo CD80/biotin (Invitrogen, reference number 13–0801, Clone 16-10A1, lot number 1934784)) was added into the BMDC suspension to achieve a final antibody concentration of 100 ng ml^{-1} and the mixture was incubated for 1 h. The BMDCs were washed once (2,000 r.p.m. for 5 min) and were subsequently incubated with 1 μg ml^{-1} streptavidin 680LT (in 1% BSA) for 40 min. Finally, the cells were washed two more times and incubated with plasmonic-fluor–680LT (extinction ~2, 200 μl) for 1 h, followed by one more wash to remove unbound plasmonic-fluor–680LT. Ten thousand cells were analysed by Guava easyCyte to acquire the fluorescence signal (RED-R channel (excitation laser 642 nm; filter 662/15 nm)) in combination with forward scatter and side scatter. The results from independent experiment are shown in the main manuscript (Fig. 6) as well as in Supplementary Figs. 46 and 47.

Statistics. For analysing the statistical difference between two groups, an unpaired two-tailed *t*-test with Welch's correction was used. For analysing the statistical difference between more than two groups, one-way analysis of variance (ANOVA) with a post-hoc Tukey's honest significance test was used. Statistical significance of the data was calculated at 95% ($P < 0.05$) confidence intervals. All values are expressed as mean ± s.d. GraphPad Prism 6 was used for all statistical analysis. We employed four-parameter logistic or polynomial fit to calculate the LOD in the standard curves of bioassays. The LOD is defined as the analyte concentration corresponding to the mean fluorescence intensity of blank plus three times of its standard deviation (mean + 3σ). Origin 2016 was employed for calculating the LOD.

Reporting Summary. Further information on research design is available in the Nature Research Reporting Summary linked to this article.

Data availability

The main data supporting the results in this study are available within the paper and its Supplementary Information. Raw imaging data (collected and analysed via the software indicated in the Reporting Summary) are available from figshare with the identifier https://doi.org/10.6084/m9.figshare.11888055.

Received: 16 January 2019; Accepted: 9 March 2020;
Published online: 20 April 2020

References

1. Cohen, L. & Walt, D. R. Highly sensitive and multiplexed protein measurements. *Chem. Rev.* **119**, 293–321 (2018).
2. Hanash, S. M., Pitteri, S. J. & Faca, V. M. Mining the plasma proteome for cancer biomarkers. *Nature* **452**, 571–579 (2008).
3. Shaw, L. M., Korecka, M., Clark, C. M., Lee, V. M.-Y. & Trojanowski, J. Q. Biomarkers of neurodegeneration for diagnosis and monitoring therapeutics. *Nat. Rev. Drug Discov.* **6**, 295–303 (2007).
4. Blennow, K. & Zetterberg, H. Understanding biomarkers of neurodegeneration: ultrasensitive detection techniques pave the way for mechanistic understanding. *Nat. Med.* **21**, 217–219 (2015).
5. Savage, M. J. et al. A sensitive aβ oligomer assay discriminates Alzheimer's and aged control cerebrospinal fluid. *J. Neurosci.* **34**, 2884–2897 (2014).
6. Westermann, D., Neumann, J. T., Sörensen, N. A. & Blankenberg, S. High-sensitivity assays for troponin in patients with cardiac disease. *Nat. Rev. Cardiol.* **14**, 472–483 (2017).
7. Rissin, D. M. et al. Single-molecule enzyme-linked immunosorbent assay detects serum proteins at subfemtomolar concentrations. *Nat. Biotechnol.* **28**, 595–599 (2010).
8. Tabakman, S. M. et al. Plasmonic substrates for multiplexed protein microarrays with femtomolar sensitivity and broad dynamic range. *Nat. Commun.* **2**, 466 (2011).
9. Zhang, B. et al. Diagnosis of Zika virus infection on a nanotechnology platform. *Nat. Med.* **23**, 548–550 (2017).
10. Zhang, B., Kumar, R. B., Dai, H. & Feldman, B. J. A plasmonic chip for biomarker discovery and diagnosis of type 1 diabetes. *Nat. Med.* **20**, 948–953 (2014).
11. Zhang, B. et al. Plasmonic micro-beads for fluorescence enhanced, multiplexed protein detection with flow cytometry. *Chem. Sci.* **5**, 4070–4075 (2014).
12. Steward, M. W. & Lew, A. M. The importance of antibody affinity in the performance of immunoassays for antibody. *J. Immunol. Methods* **78**, 173–190 (1985).
13. Roth, S. et al. Photobleaching: improving the sensitivity of fluorescence-based immunoassays by photobleaching the autofluorescence of magnetic beads (Small 3/2019). *Small* **15**, 1970016 (2019).
14. Zhang, P. et al. Ultrasensitive detection of circulating exosomes with a 3D-nanopatterned microfluidic chip. *Nat. Biomed. Eng.* **3**, 438–451 (2019).
15. Espina, V. et al. Protein microarray detection strategies: focus on direct detection technologies. *J. Immunol. Methods* **290**, 121–133 (2004).
16. Chen, Z. et al. Protein microarrays with carbon nanotubes as multicolor Raman labels. *Nat. Biotechnol.* **26**, 1285–1292 (2008).
17. Luan, J. et al. Add-on plasmonic patch as a universal fluorescence enhancer. *Light. Sci. Appl.* **7**, 29 (2018).
18. Reisch, A. et al. Collective fluorescence switching of counterion-assembled dyes in polymer nanoparticles. *Nat. Commun.* **5**, 4089 (2014).
19. Hu, J. et al. Sensitive and quantitative detection of C-reaction protein based on immunofluorescent nanospheres coupled with lateral flow test strip. *Anal. Chem.* **88**, 6577–6584 (2016).
20. Huang, L. et al. Brilliant pitaya-type silica colloids with central–radial and high-density quantum dots incorporation for ultrasensitive fluorescence immunoassays. *Adv. Funct. Mater.* **28**, 1705380 (2018).
21. Reisch, A. & Klymchenko, A. S. Fluorescent polymer nanoparticles based on dyes: seeking brighter tools for bioimaging. *Small* **12**, 1968–1992 (2016).
22. Shulov, I. et al. Fluorinated counterion-enhanced emission of rhodamine aggregates: ultrabright nanoparticles for bioimaging and light-harvesting. *Nanoscale* **7**, 18198–18210 (2015).
23. Melnychuk, N. & Klymchenko, A. S. DNA-functionalized dye-loaded polymeric nanoparticles: ultrabright FRET platform for amplified detection of nucleic acids. *J. Am. Chem. Soc.* **140**, 10856–10865 (2018).
24. Xu, Z. et al. Broad-spectrum tunable photoluminescent nanomaterials constructed from a modular light-harvesting platform based on macrocyclic amphiphiles. *Adv. Mater.* **28**, 7666–7671 (2016).

25. Kasha, M., Rawls, H. & El-Bayoumi, M. A. The exciton model in molecular spectroscopy. *Pure Appl. Chem.* **11**, 371–392 (1965).
26. Méallet-Renault, R. et al. Fluorescent nanoparticles as selective Cu (II) sensors. *Photochem. Photobiol. Sci.* **5**, 300–310 (2006).
27. Trofymchuk, K., Reisch, A., Shulov, I., Mély, Y. & Klymchenko, A. S. Tuning the color and photostability of perylene diimides inside polymer nanoparticles: towards biodegradable substitutes of quantum dots. *Nanoscale* **6**, 12934–12942 (2014).
28. Trofymchuk, K. et al. Giant light-harvesting nanoantenna for single-molecule detection in ambient light. *Nat. Photon.* **11**, 657–663 (2017).
29. Holmberg, A. et al. The biotin–streptavidin interaction can be reversibly broken using water at elevated temperatures. *Electrophoresis* **26**, 501–510 (2005).
30. Chen, H., Shao, L., Li, Q. & Wang, J. Gold nanorods and their plasmonic properties. *Chem. Soc. Rev.* **42**, 2679–2724 (2013).
31. Huang, X., Neretina, S. & El-Sayed, M. A. Gold nanorods: from synthesis and properties to biological and biomedical applications. *Adv. Mater.* **21**, 4880–4910 (2009).
32. Dreaden, E. C., Alkilany, A. M., Huang, X., Murphy, C. J. & El-Sayed, M. A. The golden age: gold nanoparticles for biomedicine. *Chem. Soc. Rev.* **41**, 2740–2779 (2012).
33. Ge, S., Kojio, K., Takahara, A. & Kajiyama, T. Bovine serum albumin adsorption onto immobilized organotrichlorosilane surface: influence of the phase separation on protein adsorption patterns. *J. Biomater. Sci. Polym. Ed.* **9**, 131–150 (1998).
34. Ashitate, Y., Tanaka, E., Stockdale, A., Choi, H. S. & Frangioni, J. V. Near-infrared fluorescence imaging of thoracic duct anatomy and function in open surgery and video-assisted thoracic surgery. *J. Thorac. Cardiovasc. Surg.* **142**, 31–38 (2011).
35. Liu, C. et al. Fluorescence-converging carbon nanodots-hybridized silica nanosphere. *Small* **12**, 4702–4706 (2016).
36. Flauraud, V. et al. In-plane plasmonic antenna arrays with surface nanogaps for giant fluorescence enhancement. *Nano Lett.* **17**, 1703–1710 (2017).
37. Tam, F., Goodrich, G. P., Johnson, B. R. & Halas, N. J. Plasmonic enhancement of molecular fluorescence. *Nano Lett.* **7**, 496–501 (2007).
38. Kinkhabwala, A. et al. Large single-molecule fluorescence enhancements produced by a bowtie nanoantenna. *Nat. Photon.* **3**, 654–657 (2009).
39. Cai, Y. et al. Photoluminescence of gold nanorods: Purcell effect enhanced emission from hot carriers. *ACS Nano* **12**, 976–985 (2018).
40. Liu, B. et al. High performance, multiplexed lung cancer biomarker detection on a plasmonic gold chip. *Adv. Funct. Mater.* **26**, 7994–8002 (2016).
41. Mayer, K. M. & Hafner, J. H. Localized surface plasmon resonance sensors. *Chem. Rev.* **111**, 3828–3857 (2011).
42. Haes, A. J., Chang, L., Klein, W. L. & Van Duyne, R. P. Detection of a biomarker for Alzheimer's disease from synthetic and clinical samples using a nanoscale optical biosensor. *J. Am. Chem. Soc.* **127**, 2264–2271 (2005).
43. Bardhan, R., Grady, N. K., Cole, J. R., Joshi, A. & Halas, N. J. Fluorescence enhancement by Au nanostructures: nanoshells and nanorods. *ACS Nano* **3**, 744–752 (2009).
44. Khatua, S. et al. Resonant plasmonic enhancement of single-molecule fluorescence by individual gold nanorods. *ACS Nano* **8**, 4440–4449 (2014).
45. Anger, P., Bharadwaj, P. & Novotny, L. Enhancement and quenching of single-molecule fluorescence. *Phys. Rev. Lett.* **96**, 113002 (2006).
46. Tian, L. et al. Gold nanocages with built-in artificial antibodies for label-free plasmonic biosensing. *J. Mater. Chem. B* **2**, 167–170 (2014).
47. Abadeer, N. S., Brennan, M. R., Wilson, W. L. & Murphy, C. J. Distance and plasmon wavelength dependent fluorescence of molecules bound to silica-coated gold nanorods. *ACS Nano* **8**, 8392–8406 (2014).
48. Mishra, H., Mali, B. L., Karolin, J., Dragan, A. I. & Geddes, C. D. Experimental and theoretical study of the distance dependence of metal-enhanced fluorescence, phosphorescence and delayed fluorescence in a single system. *Phys. Chem. Chem. Phys.* **15**, 19538–19544 (2013).
49. Yan, B. et al. Engineered SERS substrates with multiscale signal enhancement: nanoparticle cluster arrays. *ACS Nano* **3**, 1190–1202 (2009).
50. Pierre, M. C. S. & Haes, A. J. Purification implications on SERS activity of silica coated gold nanospheres. *Anal. Chem.* **84**, 7906–7911 (2012).
51. Bardhan, R., Grady, N. K. & Halas, N. J. Nanoscale control of near-infrared fluorescence enhancement using Au Nanoshells. *Small* **4**, 1716–1722 (2008).
52. Thompson, D. K., Huffman, K. M., Kraus, W. E. & Kraus, V. B. Critical appraisal of four IL-6 immunoassays. *PLoS ONE* **7**, e30659 (2012).
53. Samant, P. P. & Prausnitz, M. R. Mechanisms of sampling interstitial fluid from skin using a microneedle patch. *Proc. Natl Acad. Sci. USA* **115**, 4583–4588 (2018).
54. Mishra, J. et al. Neutrophil gelatinase-associated lipocalin (NGAL) as a biomarker for acute renal injury after cardiac surgery. *Lancet* **365**, 1231–1238 (2005).
55. Han, W. et al. Urinary biomarkers in the early diagnosis of acute kidney injury. *Kidney Int.* **73**, 863–869 (2008).
56. Munier, M. et al. Physicochemical factors affecting the stability of two pigments: R-phycoerythrin of *Grateloupia turuturu* and B-phycoerythrin of *Porphyridium cruentum*. *Food Chem.* **150**, 400–407 (2014).
57. Yuan, H., Khatua, S., Zijlstra, P., Yorulmaz, M. & Orrit, M. Thousand-fold enhancement of single-molecule fluorescence near a single gold nanorod. *Angew. Chem. Int. Ed.* **52**, 1217–1221 (2013).
58. Ma, Y. et al. Au@ Ag core−shell nanocubes with finely tuned and well-controlled sizes, shell thicknesses, and optical properties. *ACS Nano* **4**, 6725–6734 (2010).
59. Liu, K.-K., Tadepalli, S., Tian, L. & Singamaneni, S. Size-dependent surface enhanced Raman scattering activity of plasmonic nanorattles. *Chem. Mater.* **27**, 5261–5270 (2015).
60. Dixit, C. K. & Aguirre, G. R. Protein microarrays with novel microfluidic methods: current advances. *Microarrays* **3**, 180–202 (2014).
61. Jain, P. K., Lee, K. S., El-Sayed, I. H. & El-Sayed, M. A. Calculated absorption and scattering properties of gold nanoparticles of different size, shape, and composition: applications in biological imaging and biomedicine. *J. Phys. Chem. B* **110**, 7238–7248 (2006).
62. De La Rica, R. & Stevens, M. M. Plasmonic ELISA for the ultrasensitive detection of disease biomarkers with the naked eye. *Nat. Nanotechnol.* **7**, 821–824 (2012).
63. Deng, W., Xie, F., Baltar, H. T. & Goldys, E. M. Metal-enhanced fluorescence in the life sciences: here, now and beyond. *Phys. Chem. Chem. Phys.* **15**, 15695–15708 (2013).
64. Lee, K.-S. & El-Sayed, M. A. Dependence of the enhanced optical scattering efficiency relative to that of absorption for gold metal nanorods on aspect ratio, size, end-cap shape, and medium refractive index. *J. Phys. Chem. B* **109**, 20331–20338 (2005).
65. Gole, A. & Murphy, C. J. Azide-derivatized gold nanorods: functional materials for "click" chemistry. *Langmuir* **24**, 266–272 (2008).
66. Tebbe, M., Kuttner, C., Männel, M., Fery, A. & Chanana, M. Colloidally stable and surfactant-free protein-coated gold nanorods in biological media. *ACS Appl. Mater. Interfaces* **7**, 5984–5991 (2015).
67. Nedrebø, T., Reed, R. K., Jonsson, R., Berg, A. & Wiig, H. Differential cytokine response in interstitial fluid in skin and serum during experimental inflammation in rats. *J. Physiol.* **556**, 193–202 (2004).

Acknowledgements

We acknowledge support from National Science Foundation (award nos. CBET-1512043 and CBET-1900277), National Institutes of Health (R01DE027098 and R01CA141521), Center for Multiple Myeloma Nanotherapy (U54 CA199092) and a grant from the Barnes-Jewish Hospital Research Foundation (no. 3706). We thank K. Naegle for providing access to a LI-COR Odyssey CLx scanner, L. Setton for the flow cytometer, J. Rudra and T. Pietka for Luminex readers, and the Nano Research Facility (NRF) and Institute of Materials Science and Engineering (IMSE) at Washington University for providing access to electron microscopy facilities. We also thank G. Genin for inspiring discussions and suggestions.

Author contributions

S.S. and J.L. designed the project and experiments. J.L. synthesized plasmonic-fluors. A.S. and J.L. designed and performed the flow cytometry experiments of SK-BR-3 and BMDCs. R.G. performed the AFM and TEM characterization. Z.W. performed the immunocytochemistry experiment of SK-BR-3 cells and B.X. did the confocal imaging of the cells. P.R., S.C. and H.G.D. performed the SEM characterizations. R.T. performed the fluorescence lifetime measurements and analysed the data. S.A. helped to design the lifetime measurement experiments and analysed the data. J.J.M. helped to design the kidney disease-related experiments and provided the kidney disease patient samples. S.S. and J.L. wrote the paper. All authors reviewed and commented on the manuscript.

Competing interests

J.L., J.J.M. and S.S. are inventors on a provisional patent related to this technology. The technology has been licensed by the Office of Technology Management at Washington University in St. Louis to Auragent Bioscience LLC, which is developing plasmonic-fluor products. J.L., J.J.M. and S.S. are co-founders/shareholders of Auragent Bioscience LLC. These potential conflicts of interest have been disclosed and are being managed by Washington University in St. Louis. The remaining authors declare no competing interests.

Additional information

Supplementary information is available for this paper at https://doi.org/10.1038/s41551-020-0547-4.

Correspondence and requests for materials should be addressed to S.S.

nature research

Corresponding author(s): Srikanth Singamaneni

Last updated by author(s): Feb 14, 2020

Reporting Summary

Nature Research wishes to improve the reproducibility of the work that we publish. This form provides structure for consistency and transparency in reporting. For further information on Nature Research policies, see Authors & Referees and the Editorial Policy Checklist.

Statistics

For all statistical analyses, confirm that the following items are present in the figure legend, table legend, main text, or Methods section.

n/a	Confirmed	
☐	☒	The exact sample size (*n*) for each experimental group/condition, given as a discrete number and unit of measurement
☐	☒	A statement on whether measurements were taken from distinct samples or whether the same sample was measured repeatedly
☐	☒	The statistical test(s) used AND whether they are one- or two-sided *Only common tests should be described solely by name; describe more complex techniques in the Methods section.*
☒	☐	A description of all covariates tested
☒	☐	A description of any assumptions or corrections, such as tests of normality and adjustment for multiple comparisons
☐	☒	A full description of the statistical parameters including central tendency (e.g. means) or other basic estimates (e.g. regression coefficient) AND variation (e.g. standard deviation) or associated estimates of uncertainty (e.g. confidence intervals)
☐	☒	For null hypothesis testing, the test statistic (e.g. *F*, *t*, *r*) with confidence intervals, effect sizes, degrees of freedom and *P* value noted *Give P values as exact values whenever suitable.*
☒	☐	For Bayesian analysis, information on the choice of priors and Markov chain Monte Carlo settings
☒	☐	For hierarchical and complex designs, identification of the appropriate level for tests and full reporting of outcomes
☒	☐	Estimates of effect sizes (e.g. Cohen's *d*, Pearson's *r*), indicating how they were calculated

Our web collection on statistics for biologists contains articles on many of the points above.

Software and code

Policy information about availability of computer code

Data collection	Image Studio 4.0, Horiba datastation, UVProbe 2.43, LAS V4.7, guavaSoft 3.1.1, Olympus FV1000 confocal-microscope software.
Data analysis	ImageJ 1.6.0_24, NanoScope Analysis 1.5, Origin 2016, DAS6 v6.1, Image Studio Lite 5.2, GraphPad Prism 8.0.1, FV10-ASW 3.0 Viewer, FlowJo 10.5.0

For manuscripts utilizing custom algorithms or software that are central to the research but not yet described in published literature, software must be made available to editors/reviewers. We strongly encourage code deposition in a community repository (e.g. GitHub). See the Nature Research guidelines for submitting code & software for further information.

Data

Policy information about availability of data

All manuscripts must include a data availability statement. This statement should provide the following information, where applicable:

- Accession codes, unique identifiers, or web links for publicly available datasets
- A list of figures that have associated raw data
- A description of any restrictions on data availability

The main data supporting the results in this study are available within the paper and its Supplementary Information. Raw imaging data (collected and analysed via the software indicated above) are available from figshare with the identifier https://doi.org/10.6084/m9.figshare.11888055.

Field-specific reporting

Please select the one below that is the best fit for your research. If you are not sure, read the appropriate sections before making your selection.

☒ Life sciences ☐ Behavioural & social sciences ☐ Ecological, evolutionary & environmental sciences

For a reference copy of the document with all sections, see nature.com/documents/nr-reporting-summary-flat.pdf

Life sciences study design

All studies must disclose on these points even when the disclosure is negative.

Sample size	No statistical method was employed to determine the sample size, and no sample size was necessary for this study. We provided indicatations that the pFLISA detects NGAL quickly in the urine of normal individuals and in the urine of patients known to have elevated urinary NGAL.
Data exclusions	No data were excluded from the analysis.
Replication	We have replicated each experiment at least three times independently, to support all of the claims made in this manuscript.
Randomization	The samples were chosen randomly.
Blinding	The investigator was not blinded to group allocation during the experiment. Blinding was not relevant because the main purpose of the study was to test the performance of the plasmonic-fluor-enhanced fluoroimmunoassay (that is, the accuracy, required assay time and sensitivity were compared to the state-of-the-art).

Reporting for specific materials, systems and methods

We require information from authors about some types of materials, experimental systems and methods used in many studies. Here, indicate whether each material, system or method listed is relevant to your study. If you are not sure if a list item applies to your research, read the appropriate section before selecting a response.

Materials & experimental systems

n/a	Involved in the study
☐	☒ Antibodies
☐	☒ Eukaryotic cell lines
☒	☐ Palaeontology
☐	☒ Animals and other organisms
☐	☒ Human research participants
☒	☐ Clinical data

Methods

n/a	Involved in the study
☒	☐ ChIP-seq
☐	☒ Flow cytometry
☒	☐ MRI-based neuroimaging

Antibodies

Antibodies used	human IL-6 capture antibody (R&D, catalog number DY 206, lot number P173353, PART# 840113, 120-fold dilution), human IL-6 detection antibody (R&D, catalog number DY 206, lot number P173353, PART# 840114, 60-fold dilution), mouse TNF-alpha and IL-6 capture antibody which were precoated on the microbeads (R&D, catalog number LXSAMSM-03, lot number L126064, PART# 894724), mouse TNF-alpha and IL-6 detection antibody cocktail (R&D, catalog number LXSAMSM-03, lot number L126064, PART# 894666, 11-fold dilution), human kidney biomarker antibodies precoated on the NC membrane (R&D, catalog number ARY019, lot number 1311110, PART# 893967), human kidney biomarker detection antibody cocktail (R&D, catalog number ARY019, lot number 1311110, PART# 893966), anti-human HER-2/biotin (eBioscience, BMS120BT, Clone 2G11, 186281000), anti-Mo CD80/biotin (Invitrogen, 13-0801-82, Clone 16-10A1, 1934784, 5000-fold dilution), human NGAL capture antibody (R&D, catalog# DY1757, lot# P195696, PART# 844864, 120-fold dilution), human NGAL detection antibody (R&D, catalog# DY1757, lot# P195696, PART# 844865, 60-fold dilution), mouse IL-6 capture antibody (R&D, catalog# DY406-05, lot# P195781, PART# 840171, 120-fold dilution), mouse IL-6 detection antibody (R&D, catalog# DY406-05, lot# P195781, PART# 840172, 60-fold dilution)
Validation	The antibodies purchased from R&D systems have been tested for proper performance and function under their established Quality Control Testing criteria according to the certificate of analysis from the manufacturer. The anti-human HER-2/biotin and anti-Mo CD80/biotin were recommended by their provider companies for cell staining. They have been tested by Quality Control and passed internal specifications. According to the vendor, anti-human HER-2/biotin has been validated for human and anti-Mo CD80/biotin has been validated for dog, mouse, and pig. Anti-Mo CD80/biotin has been tested by flow-cytometric analysis of activated mouse splenocytes, according to the provider.

Eukaryotic cell lines

Policy information about cell lines

Cell line source(s)	Human epithelial breast cancer cells (SK-BR-3) were purchased from ATCC.
Authentication	The SK-BR-3 cell line was authenticated via STR analysis (performed by ATCC).
Mycoplasma contamination	The cell line tested negative for mycoplasma contamination (test performed by ATCC).
Commonly misidentified lines (See ICLAC register)	No commonly misidentified cell lines were used.

Animals and other organisms

Policy information about studies involving animals; ARRIVE guidelines recommended for reporting animal research

Laboratory animals	Female mice C57BL/6 (H-2b), 5-to-6 weeks of age. Female mice C57BL/6J, 9-to-10 weeks of age.
Wild animals	The study did not involve wild animals.
Field-collected samples	The study did not involve samples collected from the field.
Ethics oversight	IACUC from Washington University in St. Louis.

Note that full information on the approval of the study protocol must also be provided in the manuscript.

Human research participants

Policy information about studies involving human research participants

Population characteristics	The characteristics of the human participants are provided in the Supplementary Information.
Recruitment	Patients with imaged renal masses were recruited under IRB 201601082 for the study, and urine samples were obtained from these patients. Consent was obtained for the use of their samples for other studies. Healthy volunteers were recruited under IRB 201202051, and urine samples were obtained from these patients. There was no perceived bias in the recruitment process.
Ethics oversight	Washington University IRB 201601082 “Nanotech Biomarkers For Renal Cancer Intervention: Clinical Validation and Utility”; Washington University IRB 201202051 "Urine Proteome of Surgical Patients and Healthy Volunteers"

Note that full information on the approval of the study protocol must also be provided in the manuscript.

Flow Cytometry

Plots

Confirm that:

☒ The axis labels state the marker and fluorochrome used (e.g. CD4-FITC).

☒ The axis scales are clearly visible. Include numbers along axes only for bottom left plot of group (a 'group' is an analysis of identical markers).

☒ All plots are contour plots with outliers or pseudocolor plots.

☒ A numerical value for number of cells or percentage (with statistics) is provided.

Methodology

Sample preparation	For the isolation of BMDCs, female C57BL/6 (H-2b) mice that were 5-to-6 weeks of age were purchased from Jackson Labs (Bar Harbor, ME, USA). The mice were maintained under pathogen-free conditions. All experiments employing mice were performed in accordance with laboratory animal protocol approved by the School of Medicine Animal Studies Committee of Washington University in St. Louis. Mouse were euthanized using CO2 asphyxiation and cervical dislocation. The euthanized mouse was kept in 70% (v/v) ethanol for 1 min. Both the femurs and tibiae were isolated, and the muscle attachments were carefully removed using gauze pads. Both ends of the bones were cut with scissors and the marrow was centrifuged in an adapted centrifuge tube (0.6 ml tube with a hole inserted in 1.5 ml tube) at 1000 rpm for 10 seconds. The pellet was resuspended by vigorous pipetting in RPMI 1640 media. The cells were passed through a 70 µm cell strainer to prepare a single cell suspension. After one washing (1200 rpm, 5 min), red blood cells were depleted with RBC lysis buffer (Sigma-Aldrich). The bone marrow cells were collected and cultured in 100-mm Petri dishes containing 10 mL RPMI medium supplemented with 10% heat-inactivated FBS, 50 IU mL-1 penicillin, 50 µg mL-1 streptomycin, and 20 ng mL-1 mouse recombinant granulocyte- macrophage colony-stimulating factor (GM-CSF, R&D Systems, MN, USA). Around one million BMDCs were cultured in 6 well plates and were stimulated by adding 1 ml of different concentrations of LPS (0.5 µg/ml, 0.2 µg/ml, 0.1 µg/ml, 0.05 µg/ml, 0.01 µg/ml, and 0 µg/ml) for 24 hours. Cells were harvested using a cell scraper for further staining and flow cytometry analysis.

Instrument	Guava easyCyte
Software	Collection: guavaSoft 3.1.1; Analysis: FlowJo 10.5.0.
Cell population abundance	No sorting was performed.
Gating strategy	The cells were gated by preliminary FSC/SSC gates to exclude any dead cells or cell debris. A specific example of the gating strategy is provided in the Supplementary Information.

☒ Tick this box to confirm that a figure exemplifying the gating strategy is provided in the Supplementary Information.